J Mater Sci (2012) 47:3925–3948
DOI 10.1007/s10853-011-6213-1

ANNIVERSARY REVIEW

Materials development for intermediate-temperature solid oxide electrochemical devices

Ainara Aguadero · Lydia Fawcett · Samuel Taub · Russell Woolley · Kuan-Ting Wu · Ning Xu · John A. Kilner · Stephen J. Skinner

Received: 14 November 2011 / Accepted: 15 December 2011 / Published online: 11 January 2012

Abstract One of the major challenges in developing electrochemical devices for energy generation has been the identification and development of materials with outstanding performance at reduced (intermediate) temperatures (500–700 °C), increasing the durability and lowering the cost of the device. A solid-state electrochemical cell is in outline a simple device consisting of three components: anode, electrolyte and cathode. The function of each component is critical to cell performance, and as interest in fuel cells and electrolysers has gathered pace, many materials have been evaluated as functional components of these cells. Typically, the requirement for new materials development has been the drive to lower operation temperature, overcoming sluggish reaction kinetics in existing materials. Novel materials for the functional components of both electrolysers and fuel cells are introduced, with emphasis placed on the air electrode and electrolyte, with the potential of new classes of materials discussed, including layered materials, defect fluorites and tetrahedrally coordinated phases. Furthermore, the opportunity presented by thin film deposition to characterize anisotropic transport in materials and develop devices based on thin films is discussed.

A. Aguadero · L. Fawcett · S. Taub · R. Woolley · K.-T. Wu · N. Xu · J. A. Kilner · S. J. Skinner (✉)
Department of Materials, Imperial College London, Exhibition Road, SW7 2AZ London, United Kingdom
e-mail: s.skinner@imperial.ac.uk

A. Aguadero
Instituto de Ciencia de Materiales de Madrid, C.S.I.C, Cantoblanco Madrid 28049, Spain

Introduction

Fuel cells, as energy conversion devices, offer many advantages in comparison with traditional combustion engines, including high efficiency, low emissions and cell scalability. Under the influence of industry leaders (General Electric, Siemens, Westinghouse, Rolls Royce, etc.), solid oxide fuel cells (SOFCs) were predominantly considered and designed as large-scale stacks of multi-megawatt output for integration with gas turbines. In the early 1990s, it was recognized that the operating temperature should be lowered as far as possible within the acceptable range of electrode kinetics and internal resistance of the cell [1]. The decreased operating temperature (targeting a range of 400–700 °C) promised several advantages: (1) better long-term performance stability; (2) fewer restrictions on manifolding design, e.g., metallic separators and thinner heat insulators can be adopted; (3) faster start-up, which is essential for automobile-related applications; and (4) therefore, lower overall cost [2]. The emerging market of small-scale (1 kW to several 10 kW) SOFC applications, such as combined heat and power (CHP) systems and auxiliary power supply for automobiles, gave a tremendous stimulus to the research into intermediate-temperature SOFCs (IT-SOFCs) [3]. As a relatively new area of SOFC research, identifying optimised materials and understanding the rate-limiting mechanism(s) are still the main challenges for IT-SOFC research.

Intermediate-temperature fuel cells can operate under a wide variety of fuels (e.g., hydrogen, methane, carbon monoxide, kerosene, and biomass derived gases); however, the most efficient and environmentally friendly conversion is achieved when using H_2 as fuel. Currently, the hydrogen used in fuel cells is produced from the catalytic reformation of fossil fuels producing emission of CO_2. To achieve zero-

emission hydrogen production, the challenge is to source it from renewable clean primary energy technologies [3]. High-temperature steam electrolysis is widely accepted as a zero carbon–emitting method of producing hydrogen for SOFCs [4]. The advantage of high-temperature (up to 700 °C) solid oxide electrolysis cells (SOECs) is that they have lower electrical power requirements, increased electrode activity and higher electrolytic efficiency than the established low-temperature polymer-based cells [5, 6]. A further advantage of SOECs is that they can be reversibly used as a SOFC, producing electricity by consumption of the stored hydrogen that had been generated in SOEC mode.

In this article, the latest advances in the development of materials for solid oxide electrochemical cells for intermediate-temperature applications are presented. As this is a broad field, the review focuses on the two major areas that are of concern to developers: pure ionic conductors as electrolytes and mixed ionic-electronic conductors as air electrodes, with the main thrust being towards novel materials. This review clearly cannot be exhaustive, and the reader is directed to the many excellent reviews relating to conventional materials in SOFCs [7–9] and references therein. Before the discussion of novel materials for intermediate-temperature SOFC and/or SOEC devices in detail, a brief overview of the current technology is presented.

In a SOFC, the oxidant, usually air, is supplied to the cathode where it is electrochemically reduced. The oxygen ions generated are then transported through the ceramic electrolyte to the anode where the fuel, typically hydrogen, is oxidised. Electrons liberated at the anode flow through external connections to the cathode, completing the circuit, generating useful power. Although the fuel is typically H_2, the advantage of the SOFC is that the electrochemistry allows for alternative fuels such as reformed hydrocarbons to be used, thereby producing only water or CO_2 as the waste products. A SOEC facilitates the reverse reactions, using an external electricity supply to dissociate H_2O. In this device, at the cathode, the reduction reaction takes place producing H_2. The generated oxygen ions are transported through the electrolyte to the anode where the oxidation reaction takes place generating O_2. A schematic view of a SOFC and SOEC electrochemical device is shown in Fig. 1.

It is important to note that in both systems, the electrolyte is a dense ceramic pure ionic conductor that acts as a gas separation membrane and prevents the short circuiting of the cell. Many of the problems facing the future development of ceramic electrochemical devices can be divided into two categories relating to either materials performance or to materials processing. The predominant issues surrounding material performance relate to lowering the temperature of operation, whereas issues associated with materials processing often relate to the stack architecture.

Several stack designs have been proposed during the development of the SOFC [10]; of these, the planar design has proved the most successful for intermediate-temperature applications. Planar designs are generally configured as a series of screen-printed flat plates adjoined by interconnects. Within most IT-SOFC stack designs, these interconnects are now made from ferritic stainless steel; and result in several material-processing problems. At elevated temperatures during both manufacture and operation, elements from the stainless steel, such as Cr and Mn, can diffuse into the electrolyte or electrodes as impurities, retarding the conductivity or reaction kinetics.

To understand the challenge of choosing appropriate electrolyte materials for intermediate-temperature fuel cells in a planar configuration, in the first part of this article, we focus our attention on reviewing the different electrolyte materials typically used in devices. In particular, we focus on the effect of different metal additives on doped-ceria electrolytes as they are the most commonly used materials for intermediate-temperature applications.

Electrolyte materials for IT-SOFCs

Yttria-stabilized zirconia (YSZ) is the traditional choice of electrolyte material in SOFCs because of its high mechanical and chemical stability combined with high ionic conductivity over a wide range of temperatures and oxygen partial pressures. Reports have shown that YSZ exhibits maximum ionic conductivity close to the dopant

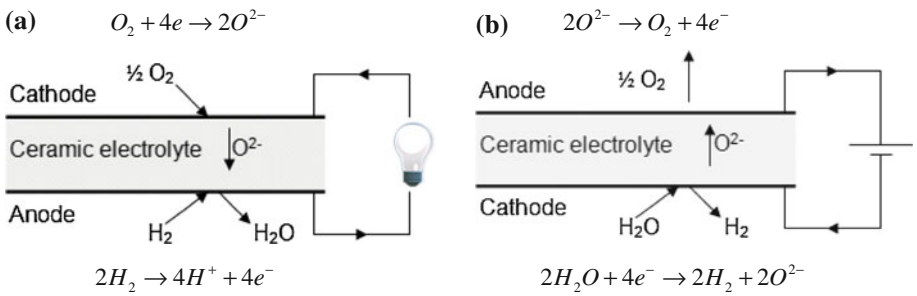

Fig. 1 Schematic diagram illustrating the basic electrochemical processes occurring at the electrodes in (**a**) a SOFC and (**b**) a SOEC

level required to fully stabilise the cubic-fluorite structure [11]. This has led to the preferential use of 8 mol% YSZ as an electrolyte material with reported ionic conductivities of $\sim$0.1 S cm^{-1} at 1000 °C [12]. The operating temperature of fuel cells based on this electrolyte is, however, considered too high for small-scale power generation, where there has been a recent impetus to lower the operating temperature to between 500 and 700 °C. These so-called IT-SOFCs allow lower cost ferritic stainless steel to be used as in cell/stack construction and in the balance of plant [13] and will reduce the problems associated with the high operating temperatures of YSZ electrolytes.

It is, therefore, necessary to consider alternative electrolyte materials that promote high ionic conductivity within this intermediate-temperature range. Among the known oxygen ion conductors, δ-phase Bi_2O_3 (a fluorite type structure) has shown the highest ionic conductivity; reportedly 1–2 orders of magnitude greater than YSZ [14]. This material is, however, only stable between its high-temperature cubic phase (α to δ transition at 730 °C) and its melting point at approximately 825 °C. Takahashi et al. [15] first demonstrated that the δ-phase could be stabilised over a wider range of temperatures using Y_2O_3 substitutions, whilst Verkerk et al. [16] reported the highest recorded conductivities for an oxygen ion conductor (2.3×10^{-2} S cm^{-1} at 500 °C) using $(Bi_2O_3)_{0.8}(Er_2O_3)_{0.2}$. Despite these high conductivities, stabilised bismuth oxide is considered impractical for use as a SOFC electrolyte because of instability under anode conditions [17].

High levels of oxygen ion conductivity have previously been reported in perovskite-type phases derived from lanthanum gallate ($LaGaO_3$), in particular the $La_{1-x}Sr_xGa_{1-y}Mg_yO_{3-\delta}$ (LSGM) series [18]. The partial substitution of lanthanum for strontium and the incorporation of divalent magnesium cations into the gallium sub-lattice increase the concentration of oxygen vacancies within the material. This results in a higher oxygen conductivity, with the highest values reported for the composition $La_{0.8}Sr_{0.2}Ga_{0.83}Mg_{0.17}O_{0.2815}$ at 700 °C [19]. However, issues concerning the reduction of gallium and the formation of secondary phases under reducing conditions [20–22] are still to be resolved. On the other hand, the LSGM electrolyte has been observed to react with Ni leading to the formation of a highly resistive phase, resulting in the degradation of the cell performance [23, 24]. Some authors observed that the use of a buffer layer such as La-doped ceria helps to minimize the reaction between Ni and LSGM, improving the performance of the cell [25, 26]. Supporting this finding, Zhang et al. investigated the sintering temperature of a Ni–ceria cermet anode on a LSGM electrolyte noting that reactivity between both species is a critical feature, finding that the anode sintered at 1250 °C displays minimum anode polarization suggesting that this sintering temperature is the optimum to deposit Ni–ceria cermets on LSGM electrolytes.

Ceria-based electrolytes (most commonly ceria–gadolinia solid solutions, such as $Ce_{1-x}Gd_xO_{2-y}$–CGO) are currently one of the preferred electrolyte materials for IT-SOFCs because of their higher ionic conductivity at lower temperature (down to 500 °C) than the competing electrolyte materials [27]. In the following section, an overview of CGO electrolytes is presented.

Cerium gadolinium oxide electrolytes (CGO)

CGO adopts the fluorite structure exhibiting high ionic conductivity, due in part to its relatively open structure and associated tolerance for atomic disorder. However, under low oxygen partial pressures and high temperature, ceria reduction will introduce electronic charge carriers and oxygen vacancies to the system. The addition of aliovalent oxides, such as gadolinium oxide (Gd_2O_3), further increases the concentration of oxygen vacancies, whilst also lowering the reducibility of the material, resulting in a material with substantial ionic conductivity.

One of the main concerns with using CGO as an electrolyte material relates to its processing, particularly its relatively poor densification behaviour, and the associated high temperatures required for sintering, which in some cases are reported to exceed 1500 °C [28]. There are two approaches which can be taken to reduce the sintering temperature; the first is to decrease the initial particle size [29], leading to an increase in the driving force for densification. The second is to introduce a sintering aid, usually a small quantity of a given transition metal oxide (TMO) to increase the sintering rate. Several TMOs have been shown to be beneficial to the sintering behaviour of CGO, although their effect on the conductivity is variable. Furthermore, metal salts have also been considered as sintering additives, although there are few reports on this aspect of materials processing [30].

Particular emphasis has been given in the literature to cobalt oxide additions, which have proven effective in promoting densification when added in concentrations greater than 0.5 mol% [31, 32]. Kleinlogel and Gauckler [31] found that nanocrystalline CGO could be sintered to greater than 99% theoretical density at temperatures as low as 900 °C using 1–2 mol% Co additions. This is illustrated in Fig. 2, which shows the maximum densification rate of CGO20 + 2 mol% Co corresponding to a temperature of $\sim$870 °C. Kleinlogel and Gauckler [33] argued that the optimum Co concentration would correspond to a temperature at which both the maximum shrinkage rate and >95% theoretical density could be achieved. By plotting these two parameters, an optimum dopant concentration of $\sim$2 mol% Co was reported. These findings are in agreement with those of Lewis [34], who found that the

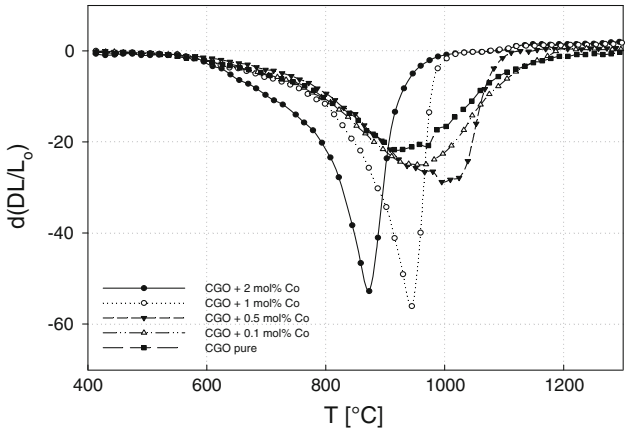

Fig. 2 Variation in linear shrinkage as a function of temperature and Co_3O_4 concentration for the CGO20 system. Image adapted from [31]

maximum enhancement to the sinterability of CGO10 would occur at 2 mol% Co. Jud et al. [35] further concluded (using electron energy loss spectroscopy—EELS) that only 0.06 mol% Co might be required to promote the enhanced sintering effects in CGO so long as the additive is distributed homogeneously.

Figure 2 shows that pure CGO exhibits a broad sintering range (~400 °C), whereas CGO + 2 mol% Co has completed the densification process within ~50 °C. Kleinlogel and Gauckler [31] explain that this is representative of solid-state sintering and liquid-phase sintering, respectively. Initial TEM analysis by these authors showed the existence of an amorphous cobalt-rich grain boundary film when the sintering was interrupted at 900 °C after 10 min. It was speculated that the film formed a liquid coating around the CGO particles at 900 °C, assisting densification through a liquid-phase sintering mechanism. HRTEM analysis later verified that after prolonged heat treatment (1400 °C for 2 h), the grain boundary film material had diffused back into the bulk. Kleinlogel and Gauckler [33] speculated that cobalt would form a liquid film at significantly lower than its eutectic temperature of 1420 °C (in the CoO–CGO system) because the melting point of a material is known to decrease with decreasing film thickness (~1–3 nm in this case). Enhanced sintering has also been previously attributed to the reduction of Co_2O_3 to CoO [33]. Lewis et al. [36] later refuted the aforementioned reports concerning the diffusion of cobalt into the grain bulk. It was shown using energy dispersive X-ray spectroscopy (EDX) that large concentrations of cobalt still existed at some grain boundaries in CGO + 2 mol% Co after sintering at 980 °C for 12 h. Lewis et al. concluded that because cobalt was only detectable at some boundaries, the film must, therefore, not entirely wet the grains. Similar observations were subsequently reported by Fagg et al. [37] in CGO20 and later by Jud et al. [35] and Zhang et al. [38] who showed the presence of cobalt at triple-points and along selected grain boundaries. Jud et al. [39] have more recently argued that cobalt oxide acts as an activator material that manifests itself in higher shrinkage rates, resulting from the formation of intergranular films. Kleinlogel and Gauckler [40] subsequently showed that adding less than 2 mol% Co would have no influence on the total conductivity of CGO when compared with the pure material.

Alternative transition metal oxide additives in CGO

Despite the emphasis given in the literature to cobalt oxide substitutions, several other transition metal oxides have been considered as possible sintering aids for CGO; of these, CuO, NiO, Cr_2O_3, Fe_2O_3 and MnO_2 have been the most thoroughly investigated. A brief discussion of these additives is presented in the following.

M^{2+} additives in CGO

Nicholas and De Jonghe [41] quite successfully predicted the sintering behaviour of several transition metal oxide additives in 10 mol% Gd-doped CeO_2 (CGO10) using a Vegard's slope quality factor based on Kim's [42] constitutive equations. Because the solubility of an additive in CeO_2 is known to be inversely proportional to the square of its Vegard's slope, and because any liquid-phase sintering aid must have limited solubility in the grain bulk, it was suggested that a dopant likely to induce liquid-phase sintering should have a Vegard's slope value much greater than zero. However, because of the formation of insoluble second phases at very high values, a 'moderate' Vegard's slope was deemed the most likely to promote liquid-phase sintering. Nicholas and De Jonghe found that Cu additions confirmed these assumptions, leading to improved densification behaviour in CGO. It was, however, reported that Ni failed to influence the sintering behaviour in either direction. These results conflicted with those of Kleinlogel and Gauckler [43] (Fig. 3), who showed that Ni would promote densification in CGO (>98%) at temperatures lower than 1100 °C. The drop in density shown in Fig. 3 for Cu and Ni at high temperature has been assigned to expansion in the samples resulting from a reduction reaction (e.g., CuO → Cu_2O). On the other hand, Avila-Paredes and Kim [44] concluded that the addition of low levels of Cu (<0.5 mol%) had very little effect on the bulk ionic conductivity of $Ce_{0.99}Gd_{0.01}O_{2-x}$, but resulted in a slight decrease in intrinsic grain boundary conduction. These findings are in agreement with Zajac et al. [45] for CGO15, although a deviation in bulk conductivity was noted with increasing Cu content. Fagg et al. [46] found no significant difference in the total conductivity of 2 mol% Cu-doped CGO20 for samples sintered between 900 and 1000 °C when compared with the pure material. Furthermore, Zajac

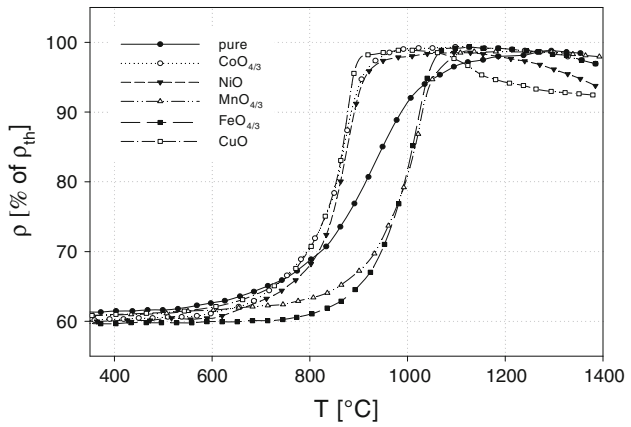

Fig. 3 Variation in density linear shrinkage as a function of temperature at constant heating rate for CGO with differing TMO dopants (2 mol% each). Image adapted from [43]

et al. [45] also reported that low-level Ni doping in CGO15 (2 mol%) had no effect on either the bulk or grain boundary conductivity for samples sintered at 1300 °C. This is in contrast to Ou et al. [47] who reported that the addition of Ni to $Sm_{0.2}Ce_{0.8}O_{1.9}$ (SDC) resulted in a total conductivity decrease. This was assigned to a high degree of oxygen vacancy ordering which resulted from Ni^{2+} being substituted for the host cations.

M^{3+} additives in CGO

Nicholas and De Jonghe [41] again used a Vegard's slope quality factor to access the suitability of several M^{3+} transition metal dopants, concluding that additions of Mn and Fe less than 5 mol% were beneficial to the sinterability of CGO10. These findings are in agreement with those of Kleinlogel and Gauckler (Fig. 3) [43] who showed that adding either Mn or Fe reduced the maximum sintering temperature; however, retarded the densification kinetics less than ~1000 °C compared with pure CGO20. Zhang et al. [48] reported that the addition of 1 mol% Mn reduced the sintering temperature of CGO20 by more than 150 °C. The authors refuted the explanation first proposed by Gauckler et al. concerning liquid-phase densification enhancements because of the low-sintering temperatures used. Instead, a viscous flow sintering mechanism was identified which was believed to increase early stage densification. This results in an increased particle contact area, leading to an increase in the diffusion flux and thus further enhances densification. A change in early stage sintering mechanism has since been supported elsewhere [49–51]. Dong et al. [50] and Zhang et al. [51] reported that the addition of 0.5–1.0 mol% Fe_2O_3 to CGO10 and CGO20, respectively reduced the maximum sintering temperature by up to 200 °C, although any further increase in the additives concentration would have little effect on the densification.

Kondakindi and Karen [52] reported a decrease in both grain boundary and total conductivity in 2 mol% Fe-doped CGO10 samples sintered between 900 and 1400 °C, although conductivity values approaching those of pure CGO10 were noted at higher temperatures. Higher conductivity values were also reported with increasing sintering temperature up to 1200 °C. Greater than this temperature, it was suggested that dissolution of Fe in the grain bulk would lower the concentration of free-oxygen vacancies leading to the formation of defect complexes. These findings are in contrast to Pikalova et al. [53] and Dong et al. [50] who reported an increase in total conductivity for 1 mol% Fe-doped CGO and Zhang et al. [51] who reported an increase in the grain boundary conductivity. This increase was assigned to the grain boundary SiO_2-scavenging effect associated with Fe. It was concluded that the optimal scavenging effect would be achieved in CGO20 with 0.5 at% Fe addition and a sintering temperature between 1400 and 1500 °C. Zhang et al. also reported a decrease in bulk conductivity which they associated with the dissolution of Fe^{3+} ions in the host material. This was believed to increase the oxygen vacancy association enthalpy because of the Fe^{3+} ions being much smaller than those of Gd^{3+}. Fagg et al. [46] again reported no significant difference in the total conductivity for 2 mol% Fe-doped CGO20 when compared with the pure material. Avilla-Paredes and Kim [44] showed that the doping of high-purity $Ce_{0.99}Gd_{0.01}O_{2-x}$ with less than 0.5 mol% Fe lowered the intrinsic grain boundary activation energy by almost 20%, resulting in a resistivity decrease of up to an order of magnitude. EELS measurements showed that the grain boundaries were free of any secondary phases, leading the authors to conclude that Fe may exist in the grain boundaries as point defects. It was hypothesised that the Fe^{3+} ions would be substituted for Ce^{4+} ions in the grain boundaries, resulting in an effective negative charge that would partially counterbalance that of the positive core. The authors argued that a net reduction in positive charge would result in a decrease in space–charge potential and hence a decrease in the energy barrier to ionic diffusion across the grain boundary.

Regarding Mn, Kondakindi and Karen [52] reported that 2 mol% Mn additions resulted in a decrease in both the total and grain boundary conductivity of CGO10 samples sintered between 900 and 1400 °C. These results are consistent with those of Pikalova et al. [49] for 1 mol% Mn-doped CGO20. Zhang et al. [48, 53] attributed this behaviour to the effect of Mn on the viscosity and wetting characteristics of SiO_2 impurities in CGO, resulting in its propagation along the grain boundaries. It was further noted that in high-purity CGO samples (i.e., those with low silica content), Mn doping alone showed little effect on the grain boundary conductivity.

Finally, Zajac et al. [45] concluded that adding Cr to CGO15 improved both the bulk and grain boundary conductivity in air for samples sintered at 1500 °C. However, they found that Cr had a detrimental effect on the conductivity with increasing additive concentration for samples sintered at 1300 °C. The effect of the Cr additive in particular is of significance as Cr poisoning of SOFC electrodes is a concern, and this decrease in conductivity could be a significant factor, particularly if composite electrodes are used.

Mixed ionic-electronic conducting electrodes for intermediate-temperature operation

As electrolytes are developed that operate at reduced temperatures, within the intermediate-temperature regime, one of the main limitations to the performance of electrochemical cells is the air electrode. Electrode performance is dictated by the reaction kinetics and transport properties of the electrode materials, and for high-temperature devices, materials that use only a triple-phase boundary (TPB) reaction mechanism offer acceptable performance. However, as temperature is reduced, TPB kinetics becomes a limiting feature of the device. To overcome this problem, a mixed ionic-electronic conductor (MIEC) is required. MIECs function effectively as IT electrodes because of the improvement of the kinetics of the oxygen reduction reaction because of the enhancement of the active area from the TPB to a double inter-phase electrode (MIEC)-air as illustrated in Fig. 4. In this case, MIEC materials provide not only the electrons for the reduction of oxygen but also the ionic conduction required to ensure the transport of the formed oxygen.

Co-based perovskites

Most of the state of the art MIEC materials belong to the perovskite-oxide family (ABO_3-type), mixed metal oxides, in which both A- and B-sites can be partially or fully substituted leading to a wide range of oxygen stoichiometries and interesting transport properties. Among them, the Co-based materials have been intensively investigated because of their suitable electrochemical properties.

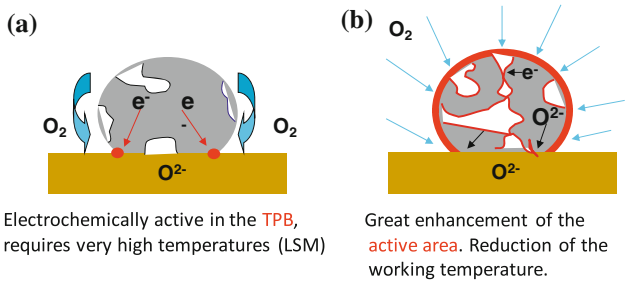

Fig. 4 Active areas for oxygen reduction electrochemical reaction in a (**a**) pure electronic conductor and (**b**) mixed ionic-electronic conductor (MIEC)

Extensive research efforts have been focused on the $LaCoO_3$-based materials that have demonstrated an excellent combination of high electronic conductivity with good ionic conductivity [54]. It is worth noting that doped $LaCoO_3$ materials were first investigated as the cathode material for high-temperature SOFCs, which benefited from their high melting point and outstanding chemical stability in oxidizing environments at high temperature (700–1000 °C) [55, 56], in combination with the previously stated electrochemical properties. Fast ion conduction is linked to the oxygen defects, and hence the oxygen non-stoichiometry of $LaCoO_3$ was firstly studied in the 1990s by Seppaene et al. [57] using a coulometric titration technique and by Mizusaki et al. [58] on single-crystal samples at high temperature (>900 °C), focussing on the defect structure as a function of oxygen partial pressure. Subsequently, Petrov et al. [59] probed the oxygen non-stoichiometry of $LaCoO_3$ using thermo-gravimetric analysis (TGA) and combined these measurements with quantitative modelling analysis [55, 56, 60, 61] of the defect structure as a function of pO_2 to provide a sound theoretical background to these experimental studies.

To explain the physics behind the promising electronic conductivity found in $LaCoO_3$, two alternative views have been promoted: itinerant or localized electrons [55, 62]. Goodenough et al. [62] and Thornton et al. [63] concluded that the electronic conduction in $LaCoO_3$ occurs through charge transfer via Co–O–Co bonds by systematically investigating the spin state of cobalt and phase transitions of the material in the temperature between 0 K and 1200 K. $LaCoO_3$ has a homogeneous metallic phase about 650 K, which contains high-spin cobalt alternating with intermediate-spin cobalt ions in an ordered array [62]. The electronic conductivity is thus attributed to the transition from fluctuating, localized Co-3d configurations in the semiconductive phase to itinerant σ states in the metallic phase. The alternative view resulted from the comparison of oxygen non-stoichiometry [56], conductivity and Seebeck coefficient [60] data obtained as a function of temperature and oxygen partial pressure with two defect models (electron/holes are itinerant or localized). From these data, it was concluded that both models fit the experimental data equally well. However, further work [61] on the defect-induced expansion of $LaCoO_{3-\delta}$ claimed that the chemical expansion model is consistent only with the localized nature of electron species, which ruled out the itinerant model and proved the existence of small polarons on the cobalt site.

Although $LaCoO_3$ has attractive electrochemical performance, concerns with mechanical stability and

reactivity with electrolytes have led to the investigation of substituted materials. These are discussed briefly in the following section.

A-site-substituted $LaCoO_3$

The introduction of an alkali earth metal to the La–Co–O system leads to the formation of solid solutions La–Me–Co–O (Me=Ca, Sr, Ba) in which partial substitution of La^{3+} for Me^{2+} leads to an increase of mean oxidation state of cobalt ions and a significant increase of oxygen deficiency [55]. During the A-site substitution procedure in $La_{1-x}Me_xCoO_{3-\delta}$, charge compensation is firstly achieved by the increase of valence of cobalt until x reaches about 0.3; for further increments of x, i.e., the Me content, oxygen non-stoichiometry increases to maintain the charge neutrality [64]. Furthermore, it is worth noting that the nature of the doped alkali earth metal does not influence the level of oxygen deficit [65, 66], although the homogeneity range for Ca, Sr and Ba is essentially different because of their different polarization properties.

It is known that important properties of doped lanthanum cobaltite such as oxide-ion and electrical conductivity in ambient atmosphere are directly related to their defect structure [56]. Among the doped lanthanum cobaltites, Sr doping has received most attention not only in this respect but also because of its excellent catalytic activity for oxygen reduction [67–69]. $La_{1-x}Sr_xCoO_{3-\delta}$ phases were suggested as promising candidates for the SOFC cathode as well as for use in oxygen separation membranes and membrane reactors for syngas production [70]. The oxygen non-stoichiometry and the defect structure were firstly studied by Mizusaki et al. [58, 71], who suggested $La_{1-x}Sr_xCoO_{3-\delta}$ cannot be a wide band gap semiconductor, i.e., the electrons were not strongly localized on Co ions. Lankhorst et al. [72–74] further investigated the defect structure of $La_{1-x}Sr_xCoO_{3-\delta}$ ($x = 0.2, 0.4, 0.7$) by high-temperature oxygen coulometric titration, and contrary to Mizusaki et al., they adopted the electron gas rigid band model to explain the experimental results, assuming that electrons created during vacancy formation are placed in broad electron bands [73]. Petrov et al. [75] and Kozhevnikov et al. [76–78], however, found that a better explanation for the experimental data can be achieved with Sehlin's [78] small polaron conduction mechanism, which takes into account the temperature-dependent reactions of charge disproportionation of the cobalt ions and trapping of polaronic carriers on defects within the crystal structure such as oxygen vacancies and dopants. Similar to the case of undoped lanthanum cobaltite, the debate over the transport mechanism has not yet been fully settled, despite extensive efforts.

In terms of ionic conductivity, Kilner et al. [79, 80] measured the oxygen diffusion rate and surface exchange coefficient of $La_{1-x}Sr_xCoO_{3-\delta}$ ($x = 0.4, 0.7$) by isotopic exchange using secondary-ion mass spectrometry (SIMS). It was found that the surface exchange is the rate-limiting step for the permeation flux through $LaCoO_{3-\delta}$ with high Sr doping. Meanwhile, Sitte et al. [81] obtained the ionic conductivity of $La_{1-x}Sr_xCoO_{3-\delta}$ ($x = 0.6$) from galvanostatic polarization experiments as a function of oxygen non-stoichiometry and temperature. They observed that the ionic conductivity shows a maximum shifting towards large oxygen non-stoichiometry values with increased temperature, which indicated a decrease in oxygen mobility caused by the formation of a vacancy-ordered structure.

Despite of all the promising properties reported above, strontium-doped lanthanum cobaltite does suffer from several problems, including reactivity with YSZ electrolytes, forming a blocking Sr_2ZrO_4 phase [82], and high thermal expansion coefficient (TEC) (19.7×10^{-6} K^{-1} [83] leading to cell failure [64, 67, 84]. Therefore, to obtain a stable structure over the operating temperature range and maintain the high oxygen deficiency, suitable B-site substitution is preferable [85].

B-site-substituted $LaCoO_3$

The substitution of a transition metal, such as Cr, Cu, Fe and Ni, for cobalt has been found to lead to an increase of oxygen non-stoichiometry and improve substantially the electrocatalytic activity of the cathodes in comparison with $LaCoO_3$ [56, 86–88]. Petrov et al. [56] concluded that copper substitution into the cobalt sub-lattice leads to the appearance of negative-charged defects on the Co site and formation of oxygen vacancies. Introducing chromium into the cobalt sub-lattice decreases the electrical conductivity and TEC, but increases the sinterability and mechanical strength. Nickel substitution, however, presents a limited stable solid solution formation range ($Ni \geq 0.4$,), but in contrast to chromium substitution, the electronic conductivity of the material increases with increasing nickel content. Hrovat et al. find an optimum composition for cathode performance when $Ni = 0.6$, finding the TEC of the ceramics in air to be 11.9×10^{-6} K^{-1} [89], but find some concerns over reactivity with electrolytes.

Whilst these materials show some promise, the most interest in the B-site-substituted phases has been with the pseudobinary system of lanthanum cobaltite and lanthanum ferrite because of the reasonably high ionic conductivity in both perovskites [90]. For iron-substituted lanthanum cobaltite ($LaCo_{1-y}Fe_yO_3$), a rhombohedrally distorted perovskite phase has been found in the concentration range between $y = 0$ and $y = 0.45$. Incorporation of iron into the cobalt sub-lattice leads to a decrease in electrical

conductivity, oxygen non-stoichiometry and therefore the ionic conductivity [91, 92]. To overcome these issues, quaternary systems with both A- and B-site substitution have been developed.

Among the quaternary candidates for SOFC cathode materials, nickel [93, 94] and iron [83] doping of strontium-doped lanthanum cobaltites have attracted most attention. Inoue et al. [93] probed $La_{0.6}Sr_{0.4}Co_{1-y}Ni_yO_3$ with a small amount of Ni doping ($y = 0$–0.02) using AC impedance spectroscopy and reported better ionic conductivity than YSZ. Goodenough et al. [95] investigated the $La_{1-x}Sr_xCo_{1-y}Ni_yO_3$ ($y \leq 0.4$) system and reported minimum polarization resistance when $x = y = 0.2$. Combining Sr A-site doping and Ni B-site doping while fixing the total doping concentration to 0.4, Hjalmarsson et al. [94] systematically studied $(La_{1-x}Sr_x)_{0.99}Co_{0.6+x}Ni_{0.4-x}O_{3-\delta}$ ($x = 0$–0.4) composition and the relation between electrochemical behaviour and structure. When $x = 0.4$, the electrodes showed a very low polarisation resistance (about 0.01 Ωcm^2 at 750 °C) and activation energy of 1.1 eV. Despite promising properties, the overall function of these materials was found to be unsatisfactory.

Tai et al. systematically studied the crystal structure, thermal expansion, oxygen stoichiometry, thermoelectricity and electrical conductivity of $La_{1-x}Sr_xCo_{1-y}Fe_yO_{3-\delta}$ (LSCF) [83, 96, 97] with low Sr and Co contents. They found Co ions on the B-site have a smaller binding energy for oxygen than Fe: Increasing Fe content thus decreases the degree of oxygen deficiency particularly at lower temperatures. These ceramics, however, are beneficial in presenting a reduced thermal expansion coefficient (e.g., $x = 0.3$, $y = 0.8$, TEC $= 14.6 \times 10^{-6}$ K^{-1} [96]), which fulfils the requirement of thermomechanical compatibility with CGO electrolytes [83, 96, 98]. To balance the ionic conductivity and thermomechanical stability of LSCF, Tai et al. [83, 96], Stevenson et al. [99] and Petric et al. [100] compared the electrochemical performance and thermomechanical stability among a full range of compositions ($0 \leq x \leq 0.4$, $0 \leq y \leq 1$). The optimized compositional region for transport properties was reported as between $0.2 \leq x \leq 0.4$ and $y \leq 0.5$. However, a sacrifice has to be made by choosing a composition outside of this optimized region when taking thermomechanical properties into account. LSCF6428 ($La_{0.6}Sr_{0.4}Co_{0.2}Fe_{0.8}O_{3-\delta}$) exhibits the most balanced performance in this respect [83, 96, 97, 99, 100] with high electronic conductivity (340 S cm^{-1} at 550 °C [96]), high ionic conductivity (0.1 S cm^{-1} at 800 °C [101]) and a low TEC value (15.3×10^{-6} K^{-1} [96]). To further boost ionic conductivity especially for decreased operation temperature, Kilner et al. [102] and Wang et al. [103, 104] mixed $Ce_{0.8}Gd_{0.2}O_{1.9}$ into LSCF to form composite cathodes, which then effectively decreases the area-specific resistance (ASR) and further reduce the TEC value closer to that of CGO.

$SrCoO_{3-\delta}$ derivatives

The high-temperature $SrCoO_{3-\delta}$ phase has been reported to present mixed conductivity with very high oxygen permeability and electrical conductivity values [105–107]. However, at room temperature and normal pressure, $SrCoO_{3-\delta}$ oxides show different polymorphs as a function of the synthesis conditions. When the samples are quenched from the reaction temperature ($\sim$1000 °C), an orthorhombic brownmillerite-type structure is obtained. In this metastable phase, the oxygen vacancies are long-range ordered in layers of isolated MO_4 tetrahedral zigzag chains, alternating with octahedral layers [108]. On the other hand, when the samples are slowly cooled from the reaction temperature, a hexagonal polymorph is obtained [109]. Battle et al. showed that the crystal structure of the hexagonal phase could be described as a face-sharing arrangement of CoO_6 octahedra [110–112], whereas Harrison et al. [113] show that this polymorph is slightly Co-deficient, with the $Sr_6Co_5O_{15}$ chemical stoichiometry. This hexagonal phase presents very low values of oxygen permeability [105] and at temperatures greater than 900 °C undergoes a phase transition to a cubic C-perovskite with abrupt changes in the thermal expansion coefficient [107]. The stabilization of the 3C perovskite framework has been a widely used strategy to obtain an adequate mixed ionic-electronic conductor in air at intermediate temperatures. For this purpose, several chemical substitutions have been performed within the $SrCoO_3$ system either in the Sr or in the Co positions. Several studies have demonstrated that while cation substitution is necessary to stabilize the high oxygen permeable 3C perovskite, the dose of the substitution should be minimized to avoid degradation of the electrochemical properties. Nagai et al. [114] report that a rise in the valence of the substitutional cation increases the oxygen content and enhances the stability of the 3C structure. Furthermore, the doping with different cations such as Bi, Zr, Ce, Sc, Y Al and Zn in the $SrCo_{0.95}Co_{0.05}O_{3-\delta}$ has shown that elements with d^{10} configuration predominantly favours the formation of a 2H-hexagonal structure while the use of cations with p^6 configuration favours the formation of a 3C perovskite or a brownmillerite structure [115].

Nb doping leads to a highly stable perovskite with a high permeability value of 4.24 cm^3 min^{-1} cm^2 at 900 °C. Subsequent studies [116] on $SrCo_{1-x}Nb_xO_{3-\delta}$ showed that the $x = 0.1$ composition exhibits the highest electrical conductivity with a relatively low thermal expansion coefficient (TEC) of 19.1×10^{-6} K^{-1}. The area-specific resistance of this composition with a $La_{0.8}Sr_{0.2}Ga_{0.8}Mg_{0.2}O_{3-\delta}$ (LSGM) electrolyte was reported to be 0.083 Ω cm^2 at 700 °C while the performance decreases with increasing Nb content. A similar trend was observed

for the Sb-doped $SrCo_{1-x}Sb_xO_{3-\delta}$ system for which the stabilization of a tetragonal *P4/mmm* structure was firstly reported for $x = 0.1$ [117]. Later studies showed that when Sb content increases in the $x = 0.05$–0.2, at $x = 0.2$ a phase transition takes place and the material is defined in the cubic *Pm-3m* space group. In comparison with the undoped hexagonal $SrCoO_3$ phase, the obtained compounds present high thermal stability, great enhancement of the electrical conductivity and lower polarization resistances, less than 0.09 Ω cm^2 at 750 °C [118]. For this series, the stabilization of a 3C perovskite structure with corner-sharing CoO_6 octahedra relies on the presence of highly charged Sb^{5+} cations distributed over the B-site octahedral positions, preventing the highly repulsive conformations derived from the face-sharing octahedra of the hexagonal 2H polytypes. The composition with $x = 0.05$ shows the lowest ASR values ranging from 0.009 to 0.23 Ω cm^2 in the 900–600 °C temperature interval on a $Ce_{0.8}Nd_{0.2}O_{2-\delta}$ electrolyte and of 0.115, 0.069 and 0.045 Ω cm^2 for temperatures of 750, 800 and 850 °C with the LSGM electrolyte. The single fuel cell test of this composition with LSGM electrolyte and Sr_2MgMoO_6 anode gave maximum power densities of 511 and 618 mW/cm^2 at 800 and 850 °C, respectively, using pure H_2 as the fuel and air as oxidant. The good performance of this material is related to its mixed electronic-ionic conduction (MIEC) properties, which can be correlated to the investigated structural features: The Co^{3+}/Co^{4+} redox energy at the top of the O-2p bands accounts for the excellent electronic conductivity, which is favoured by the corner-linked perovskite network. The considerable number of oxygen vacancies, with the oxygen atoms showing high displacement factors (4–6 $Å^2$ in the 700–850 °C range), suggests a significant ionic mobility with a thermal expansion coefficient of around 19×10^{-6} K^{-1} in the usual working conditions in a SOFC cathode [119]. In the $SrCo_{1-x}Ti_xO_{3-\delta}$ system, the best behaviour was also achieved by the sample with lowest substitution, $x = 0.05$, with electrical conductivities as high as 160 S cm^{-1} at 800 °C and polarization resistance as low as 0.084 Ω cm^2 at 700 °C. However, the thermal expansion coefficient for this system was higher than that observed for the Sb-doped samples with values around $23 \times 10^{-6}K^{-1}$ under the usual working conditions [120]. Zeng et al. have also studied doping with Sc that leads to a mixed ionic-electronic conductor with high oxygen permeation fluxes [121] and a polarization resistance of 0.25 Ω cm^2 at 600 °C with a $Sm_{0.15}Ce_{0.85}O_{2-\delta}$ electrolyte [122]. Recently, the stabilization of a cubic perovskite with high oxygen permeation flux was also observed in the $SrCo_{0.9}Ta_{0.1}O_{3-\delta}$ phase [123]. $SrCo_{0.8}Fe_{0.2}O_{3-\delta}$ (SCFO) was found to display the highest rate and the lowest onset temperature of oxygen permeation in the $La_{1-y}Sr_yCo_{1-x}Fe_xO_{3-\delta}$ system by Teraoka et al. [124].

Doping in the Sr position with rare earths also promotes the stabilization of highly conductive perovskites. Samarium-doped cobaltite $Sm_{1-x}Sr_xCoO_{3-\delta}$ (SSC) reaches its highest conductivity (10^3 S cm^{-1}) value at $x = 0.5$ [125, 126]. However, for this composition, the thermal expansion coefficient is still greater than 20×10^{-6} K^{-1} significantly greater than all common electrolytes. Whilst this is an encouraging material, it was also found that the highest performance materials were obtained with substitution of both A- and B-sites.

Among all the cobaltite–ferrite perovskites, the $Ba_{0.5}Sr_{0.5}Co_{0.8}Fe_{0.2}O_{3-\delta}$ (BSCF) composition has been the most extensively studied. Shao et al. [127] report that the introduction of barium into SCFO not only stabilized the perovskite structure under lower oxygen partial pressures but also increased the oxygen permeation flux from that of SCFO under air/He oxygen partial pressure gradient. Subsequently, Haile and Shao [128] reported the BSCF as a very promising cathode material for intermediate-temperature applications. High power densities were achieved (1010 mW cm^{-2} at 600 °C) when using a thin film of samarium-doped ceria as an electrolyte, and the suitability of BSCF as an electrode in a single-chamber fuel cell was also probed. On the other hand, an exhaustive study of a series of compounds with $X_{0.5}Sr_{0.5}Co_{0.8}Fe_{0.2}O_{3-\delta}$ (X = Ba, La and Sm) composition that was tested as SOFC electrode materials on $La_{0.9}Sr_{0.1}Ga_{0.8}Mg_{0.2}O_{2.85}$ (LSGM) electrolytes showed that $Ba_{0.5}Sr_{0.5}Co_{0.8}Fe_{0.2}O_{3-\delta}$ (BSCF) possesses the lowest ASR values in air (0.04 Ω cm^2 at 800 °C) [129]. However, further studies on BSCF show that the high oxygen diffusion through the material responsible for its impressive performance is also accompanied by a high value of thermal expansion coefficient (20×10^{-6} K^{-1}) [130]. Furthermore, it has been observed that BSCF shows thermal instability because of a phase transformation from the cubic to a mixture of cubic and hexagonal phases in long-term studies at temperatures less than 850 °C [131, 132]. Recently, Yang et al. [133] evidenced by X-ray diffraction and transmission electron microscopy measurements that the phase transformation takes place on slow cooling between 900 and 700 °C to a mixture of cubic, hexagonal and rhombohedral phases. Furthermore, it has been observed that BSCF is susceptible to be poisoned by CO_2 at temperature ranges of 450–750 °C [134]. Figure 5 shows that in general, Co-based perovskites have superior performance with ceria-based electrolytes when compared with LSGM electrolytes with $Ba_{0.5}Sr_{0.5}Co_{0.8}Fe_{0.2}O_3$, $Sr_{0.9}Sc_{0.1}CoO_3$ and $SrCo_{0.95}Sb_{0.05}O_3$ compositions showing the lowest ASR.

Non-Co-based perovskites

Co-based perovskites present very high values of electrical conductivity and oxygen permeation leading to very low

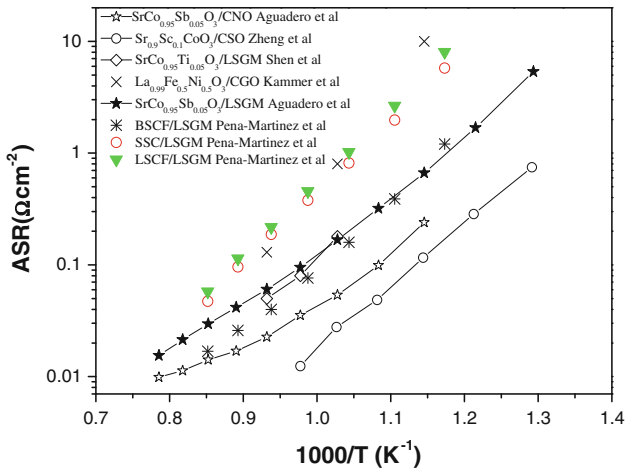

Fig. 5 Arrhenius plots of the area-specific resistance of cobalt-containing perovskites with ceria-based and lanthanum gallate–based electrolytes

values of polarization resistance at intermediate temperatures, and are therefore of interest as electrodes. Despite their attractive performance, Co-based compounds present several difficulties in practical operation, and therefore attention is now directed towards non-Co-containing materials.

Lanthanum ferrite derivatives ($LaFeO_3$) have shown promising performance with reduced reactivity compared with cobalt-based perovskites with 8% Y_2O_3-doped ZrO_2 (YSZ) electrolytes. In this material, the electrical conductivity takes place through the hopping of small polarons associated with the presence of Fe^{4+}. The partial substitution of La by an alkaline earth, A^{2+}, increases the Fe^{4+} content increasing the electrical conductivity in the system [135, 136]. Furthermore, Ralph et al. showed an improvement of the cathode performance by the partial substitution of La by Sr in $La_{0.8}Sr_{0.2}FeO_3$ reaching polarization resistance values of 0.1 Ω cm^2 at 800 °C [137]. In the $R_{0.5}A_{0.5}FeO_{3-\delta}$ (R = rare earth, A = Sr, Ca or Ba) system, it has been observed that the cathode performance and electrical conductivity increases with the increment of the alkaline-earth ionic radius [138]. On the other hand, Vidal et al. studied the effect of the doping level in the $R_{1-x}A_xFeO_{3-\delta}$ system keeping the average cation radius and the cation size mismatch in the $R_{1-x}A_x$ position of the perovskite fixed finding no clear influence of the substitution level on the electrochemical performance of these materials [139].

The introduction of aluminium into $LaFe_{1-x}Al_xO_3$ was found to decrease the electrical conductivity and not favour the creation of oxygen vacancies. However, substitution with Sr in the lanthanum position has been observed to increase the formation of oxygen vacancies and also increase the conductivity that is associated with the increasing Fe^{4+}/Fe^{3+} ratio into the crystal structure [140]. Gallium substitution ($La_{0.7}Sr_{0.3}Fe_{1-x}Ga_xO_{3-\delta}$) was found to decrease the thermal expansion of the system because of the stabilization of oxygen stoichiometry and thus decreasing chemical expansion [141]. More recently, Juste et al. show that while Ga has a stabilizing effect on the TEC, it does not adversely influence the oxygen permeation flux. They also report a strong influence of Sr content on the oxygen vacancy concentration and thus in the chemical expansion coefficient that mainly occurs at high temperatures (>870 °C), which also has a positive influence on the oxygen permeation values [142].

$LaNiO_{3-\delta}$ is also a potential MIEC cathode material but is only stable at temperatures less than 850 °C, which severely limits its technological application. The stabilization of the nickelate perovskite at higher temperatures has been a widely used strategy to obtain a suitable cathode material. Among the different dopants in the $LaNi_{1-x}B_xO_3$ system (B = Al, Cr, Mn, Fe Co and Ga), Chiba et al. found that the $LaNi_{0.6}Fe_{0.4}O_3$ composition displays the highest electrical conductivity (580 S cm^{-1} at 800 °C) and relatively low thermal expansion coefficient (11.4×10^{-6} K^{-1}) that matches with that of the SOFC electrolytes [143]. In the $LaNi_{1-x}Fe_xO_3$ ($x = 0.2$–0.5) system, the thermal expansion and the oxygen permeability was found to increase with the Ni content [144]. The $x = 0.4$ composition was also found to display the highest electrochemical performance along the $LaNi_{1-x}Fe_xO_3$ series with area-specific resistance measured as 5.5 Ω cm^2 at 600 °C using a $Ce_{0.9}Gd_{0.1}O_{2-\delta}$ electrolyte [145] (Fig. 5), which is unfortunately significantly higher than Co-containing perovskites.

In the $La_{1-y}Sr_yFe_{1-x}Ni_xO_{3-\delta}$ ($x = 0.1$–0.4, $y = 0.1$–0.2) system, the introduction of Ni^{2+} in the iron position has been observed to increase the electrical conductivity but lower the ionic conductivity because of its tendency to create clusters with the oxygen vacancies and thus decreasing their mobility. On the other hand, the incorporation of Sr^{2+} increases oxygen deficiency and ionic transport and also decreases the thermodynamic stability. The Ni-doped ferrites seem to display lower thermal expansion coefficients ($T \geq 870$ °C) than the Ga-doped oxides with values that range from 14.2 to 18.0×10^{-6} K^{-1}, rising with Ni and Sr content [146].

Ruddlesden–Popper Type Phases

Ruddlesden–Popper type materials have recently attracted significant attention as emerging alternatives to conventional perovskites for use as promising cathode materials for the next generation of intermediate-temperature SOFCs (IT-SOFCs) [147–149]. The RP series of layered oxides, generally formulated $A_{n+1}B_nO_{3n+1}$ (typically $n = 1$, 2 and 3), consists of n consecutive ABO_3 perovskite layers, alternating with AO rock-salt layers, stacking along the

crystallographic *c*-axis. Such layered MIECs display diverse defect chemistry, allowing non-stoichiometric defect structures (hypo- and hyper-stoichiometry) because of their oxygen content through tailoring A- and B-site compositions. This feature makes these oxides very attractive for the fine-tuning of their electrical and electrochemical properties [148–160]. For the case of oxygen hyper-stoichiometry, the excess oxygen can occupy interstitial sites within the AO rock-salt layers. A typical example is $La_2NiO_{4+\delta}$, which possesses the well-known K_2NiF_4-type structure. The oxygen interstitial sites in the compound are centred in the tetrahedron of surrounding metal La cations [161] (see Fig. 6). An electric field exists between the $(La_2O_2)^{2+}$ and the $(NiO_2)^{2-}$ layers so that most of the interstitial oxide-ions may be attracted to the LaO layers by the Coulomb potential, resulting in anisotropic diffusion behaviour [162]. Sayagués and his co-workers [163] have experimentally confirmed the presence of the excess oxygen and observed it to order at low temperature using high-resolution transmission electron microscopy (HRTEM). There are extensive studies and evidence of anisotropic properties in K_2NiF_4-type materials. A number of groups have confirmed the anisotropic diffusion between the *c*-axis and *ab*-axis-directions by means of a SIMS technique to determine the oxygen tracer diffusion properties in a number of K_2NiF_4-type compounds: polycrystalline $La_{2-x}NiO_{4+\delta}$ and $La_2Ni_{1-x}Co_xO_{4+\delta}$ [164, 165], single-crystalline $La_2NiO_{4+\delta}$ and $La_{2-x}Sr_xCuO_{4+\delta}$ [160, 166] and epitaxial $La_2NiO_{4+\delta}$ films [167]. Compared with these experimental investigations of $La_2NiO_{4+\delta}$, a series of theoretical studies were reported by Minervini, Frayret and Chroneos [168–170]. For example, Minervini et al. [170] investigated the accommodation and migration of excess oxygen by atomic-scale computer simulation. According to their results, the oxygen diffusion would be strongly anisotropic with activation energies of $E_a(\perp a,b) = 2.9$–3.5 eV and $E_a(\|a,b) = 0.3$–0.9 eV, depending on O^{2-} or O^- diffusion species. It is worth noting that such oxygen excess materials are the most interesting for SOFC cathode applications because they are much simpler than the substituted materials and show significant anisotropic oxygen transport as a result of their layered structure.

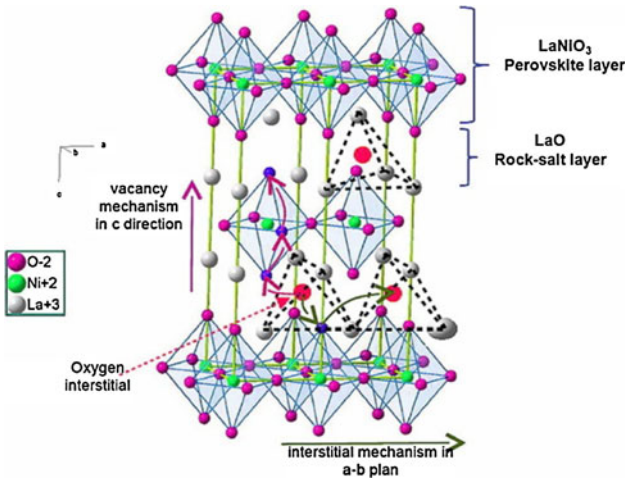

Fig. 6 Schematic diagram of the La_2NiO_4 structure showing the vacancy and interstitialcy ionic transport directions and $LaNiO_3$ perovskite and LaO rock-salt layers are indicated (adapted from [242])

However, for potential application as a cathode in operation at intermediate temperature (500 ~ 700 °C), previous research has demonstrated that $La_2NiO_{4+\delta}$-based materials are predominant electronic conductors with very promising ionic conductivity ($\sigma_i = \sim 10^{-2}$ S cm^{-1}) and acceptable electronic conductivity ($\sigma_e = 10$–100 S cm^{-1} at 327–827 °C), compared with the conventional cathode materials: strontium-doped lanthanum manganite ($\sigma_e = \sim 240$ S cm^{-1} at 800 °C; $\sigma_i = \sim 10^{-4}$–10^{-7} S cm^{-1} at 800–1000 °C) and cobaltite ($\sigma_e = \sim 1300$–1600 S cm^{-1} at 800 °C; $\sigma_i = 0.093$–0.76 S cm^{-1} at ~800 °C) [171–174]. In addition, long-term stability and compatibility of $La_2NiO_{4+\delta}$ with lanthanum gallate based and CGO electrolytes have been reported by Amow et al. [148, 149] and Sayers et al. [175], respectively. For instance, a Ni^{2+}/Ni^{3+} impurity phase formed when $La_2NiO_{4+\delta}$ were heated at 900 °C for 2 weeks in air [148, 149]. Thus, $La_2NiO_{4+\delta}$ phases are not ideally suited for practical utilization for IT-SOFCs.

Apart from the La_2NiO_4, the high-order RP-phases, $La_3Ni_2O_7$ ($n = 2$) and $La_4Ni_3O_{10}$ ($n = 3$) are of interest for use as SOFC cathodes owing to their good long-term stability and compatibility, promising electrode performance and superior electrical conductivity in operation at intermediate temperature. There was no evidence of formation of significant impurities when $La_3Ni_2O_7$ and $La_4Ni_3O_{10}$ were aged at 900 °C for 2 weeks in air [148, 149]. Amow et al. [149] studied symmetrical cells of these materials with LSGM as the electrolyte, and found that area-specific resistance (ASR) decreased with increasing *n* values with $La_4Ni_3O_{10-\delta}$ ($\delta = 0.22$) showing the lowest ASR value (~1 Ω cm^2) at 800 °C. Also, they comment that the trend of decreasing ASR with *n* apparently correlates with the increasing electrical conductivity with increasing *n*, but it might be that the trend is also related to the systematic oxygen deficiency (δ) with the *n* values, meaning that the more vacant oxygen sites in the perovskite layers, the greater the improvement of the oxygen ionic conduction. However, the latter viewpoint needs to be further investigated by means of oxygen tracer diffusion and isotope surface exchange measurement with SIMS, and even by using neutron diffraction analysis to understand the distribution of oxygen vacancies in the series of compounds. In addition, despite $La_4Ni_3O_{10-\delta}$ displaying the

lowest ASR of $\sim 1\ \Omega\ cm^2$ at 800 °C, this value is still higher than the desired value of 0.15 $\Omega\ cm^2$ reported by Steele and Heinzel [1]. Amow et al. comment that the electrode performance of the higher-order RP-phases $La_{n+1}Ni_nO_{3n+1}$ ($n = 2$ and 3) could be improved by optimising their density, microstructure and thickness.

More recently, Pérez-Coll et al. [156] investigated the electrode/electrolyte polarization properties of La_2NiO_4 and $La_3Ni_2O_7$ as cathodes on a symmetrical cell with samarium-oxide-doped ceria $Ce_{0.8}Sm_{0.2}O_{2-\delta}$ (SDC) + 2% Co as the electrolyte at 700–900 °C, reporting that the ASR of $La_3Ni_2O_{7-\delta}$ is lower than that of $La_2NiO_{4+\delta}$. Furthermore, Takahashi et al. [147] reported a single fuel cell performance test regarding the $n = 1$, 2 and 3 members of RP-phase lanthanum nickel oxides at 500–700 °C, composed of Ni–SDC//SDC//$La_{n+1}Ni_nO_{3n+1}$ ($n = 1$, 2 and 3) as an anode, electrolyte and cathode, respectively. The authors found that the ohmic and overpotential losses decreased with an increase in n value even though the catalytic activity increased with decreasing n, and $La_4Ni_3O_{10}$ exhibited better cathode properties than those of the lower members at 700 °C. Maximum power density of the cell was reported as 10.2, 36.5 and 88.2 mW cm^{-2} at 500, 600 and 700 °C, respectively. The power density values are still relatively low in comparison to conventional perovskite cathodes, but show some promise for future materials development.

Alternative non-perovskite materials

As the properties of perovskite-based SOFC cathodes have been further and further optimised, there has been a growing consensus that they may be approaching their limits of performance and that the next generation of SOFCs require cathodes based on alternative structures, such as the pyrochlores, tetrahedrally coordinated materials and those related to Bi_2O_3.

Pyrochlore-structured ruthenates

Pyrochlore-structured ruthenate oxides, general formula $A_2B_2O_7$, have long been known to have good electronic conductivity as well as catalytic activity towards oxygen reduction and hence are a natural choice for consideration as novel cathode materials. $Bi_2Ru_2O_7$ has been the most extensively studied pyrochlore compound with regard to possible SOFC applications. It is interesting, therefore, that in an early study, Bae et al. [176] found it to react with CGO after heating at 800 °C for 30 h and hence discounted it from further investigation. Subsequent studies, however, have found bismuth pyrochlores to be unreactive with CGO and other electrolytes. Jaiswal et al. [177] found no reaction after heating at 850 °C for 10 h, no reaction was seen with SDC after 100 h at 750 °C [178], and it is also unreactive with YSZ at 900 °C for 96 h [179]. Jaiswal [177] evaluated the bismuth pyrochlore as part of a symmetrical cell with CGO and found ASR values of 55.64 and 1.45 $\Omega\ cm^2$ at 500 and 700 °C, respectively. Studying a test cell of SDC/NiO|SDC|pyrochlore, Zhong et al. were able to reduce the ASR by partially substituting ruthenium for bismuth; an ASR of $<1\ \Omega\ cm^2$ at 600 °C for $Bi_2Ru_{1.6}Bi_{0.4}O_7$ was observed [178]. Suggested reasons for this improvement were that this compound densifies more readily than $Bi_2Ru_2O_7$, and that the replacement of some Ru^{4+} by Bi^{3+} could lead to a greater number of oxygen vacancies leading to improved ionic conductivity. Takeda et al. [179] have tested $Bi_2Ru_2O_7$ with YSZ and have found good cathode performance at temperatures as low as 800 °C.

Other pyrochlore compounds studied include the lead-analogue $Pb_2Ru_2O_7$. Bae [176] found this to react with CGO after 30 h at 880 °C. Doshi et al. found $Pb_2Ru_2O_7$ to decompose at 500 °C on a CGO electrolyte when the cathode overpotential of the test cell exceeded 250 mV. SEM observations indicate that molten lead was formed that percolated into the electrolyte [180]. These data, along with the well-known issues of lead toxicity, lead to the conclusion that there is perhaps little value in further studies on $Pb_2Ru_2O_7$. Doping has been used to improve pyrochlore cathode performance; a 100× reduction in ASR was seen from $Y_2Ru_2O_7$ ($\sim 4000\ \Omega\ cm^2$ at 627 °C) on doping with 5 mol.% SrO to form $Y_{2-x}Sr_xRu_2O_7$ (47 $\Omega\ cm^2$ at 627 °C) [176]; however, the improved value still falls far short of what is required for an effective cathode material and is at least an order of magnitude too high.

More recent studies have focussed on the material properties of pyrochlore compounds in isolation. Díaz-Guillén et al. [181] synthesised $Gd_{2-x}La_xZr_2O_7$ ($x = 0$–1) solid solutions and investigated their conductivities. EIS data found that the ionic conductivity of this was unaffected by the amount of lanthanum doped into the system, at least up to $x = 0.8$, with a value of 5×10^{-3} S cm^{-1} at 800 °C. Increasing the lanthanum content from $x = 0$ to 0.8 leads to increased structural ordering, therefore, fewer mobile charge carriers, however a concurrent decrease in the DC activation energy was found, the balance of the two effects explaining the lack of change seen in the ionic conductivity.

Martínez-Coronado et al. [182] evaluated R_2RuMnO_7 (R = Tb, Dy, Ho, Er, Tm, Yb, Lu and Y) and using neutron diffraction data suggested that the smaller the R, the greater the disorder of Mn over its two crystallographic sites as is observed in Fig. 7. This leads to an increased number of oxygen vacancies because of the different oxidation states of manganese on these sites, indicating that an increase in the ionic conductivity may be expected for compounds with small R. It should be noted that the findings of Díaz-Guillén [181] could apply to this case, i.e.,

the concentration of oxygen vacancies may not necessarily be proportional to ionic conductivity if other effects, e.g., order/disorder, concurrently occur. The compounds displayed semiconductor-like behaviour with conductivities ranging from 2.1 to 6.6 S cm^{-1} at 750 °C. These values are somewhat lower than is typically desired for an SOFC cathode and so the compounds may need to be formed into composites with materials with better electronic conductivity if they are to show useful performance.

Tetrahedrally coordinated cobalt compounds (Td-Co)

As previously discussed, the current IT-SOFC cathode material, LSCF, suffers from a high TEC, resulting in mechanical failures, which is ascribed to the presence of octahedrally coordinated Co^{3+} that has a facile low-spin/high-spin transition [183]; tetrahedrally coordinated cobalt does not suffer from this problem. Hence, phases with exclusively tetrahedral cobalt, denoted 'Td-Co' phases in this review, are a sensible choice for potential SOFC applications.

The bulk of the work on the Td-Co compounds has been carried out by Kim and Manthiram [184–187]. Initially, they screened a large number of such compounds to investigate which had sufficient long-term stability at high temperatures [184]; $RBa(Co,M)_4O_7$ (R = Y, Ca, In and M = Zn, Fe, Al) were synthesised and heated at ~900 °C for >50 h. It was found that only $YBaCo_{4-x}Zn_xO_7$ ($0 \leq x \leq 2.0$) was sufficiently stable under such conditions for potential SOFC use. This compound was tested for reactivity at 1000 °C/3 h with electrolyte materials CGO, LSGM and YSZ and was found to be unreactive with CGO but reactive with the latter two. Further testing at 1100 °C/2 h with CGO also found no reaction. This leads to the conclusion that CGO would be the natural electrolyte of choice for this particular Td-Co compound; however, if it was required to be used with LSGM or YSZ, a CGO barrier layer could be employed.

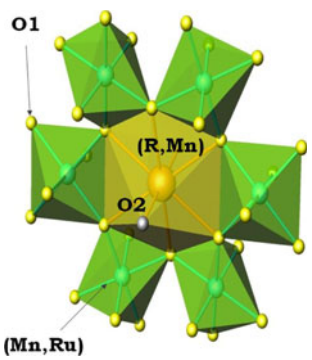

Fig. 7 Coordination environments of the two cation sites in the pyrochlore R_2RuMnO_7 structure with the possible Mn disproportionation in both crystallographic sites illustrated

The Td-Co materials were tested as cathodes of both symmetrical cells with CGO and electrolyte-supported test cells of Ni+CGO|LSGM. Given the low oxygen permeation flux that had been found, composite cathodes of Td-Co+CGO 50:50 wt% were employed, and it is not surprising that this led to improved performance over phase-pure Td-Co cathodes. For example, the polarisation resistance of $YBaCo_3ZnO_7$ symmetrical cells was 0.40 Ω cm^2 at 600 °C and 0.15 Ω cm^2 at 700 °C which was improved approximately twofold in $YBaCo_3ZnO_7$+CGO with 0.22 and 0.06 Ω cm^2 at the respective temperatures. This enhanced performance is attributed to the increased TPB length and improved oxide-ion conductivity through the CGO areas of the composite cathode. The maximum power density of this composite cathode as part of an electrolyte-supported test cell $YBaCo_3ZnO_7$+CGO|LSGM|CGO|Ni+CGO at 800 °C was 528 mW cm^{-2} which compares well to traditional perovskite-based cobalt-containing materials such as LSCF, and is significantly better than the non-Co-containing perovskites discussed earlier. In all cases, $YBaCo_3ZnO_7$ was found to be a better Td-Co compound than those with greater zinc content because of its better electronic conductivity. Kim and Manthiram [185] attempted to optimise the composite cathode by testing a range of compositions of $YBaCo_3ZnO_7$+CGO from 0 to 70 wt% CGO and found that the 50:50 composite that they had originally tested was the optimum. An anode-supported test cell of composition $YBaCo_3ZnO_7$|$YBaCo_3ZnO_7$+CGO|CGO|YSZ|Ni+CGO was made and an improved maximum power density of 520 and 743 mW cm^{-2} at 700 and 750 °C was observed.

Kim and Manthiram [186] also studied $InBaCo_{4-x}Zn_xO_7$ in a similar manner to $YBaCo_{4-x}Zn_xO_7$. Materials with $1.0 \leq x \leq 2.0$ were found to have sufficient thermal stability for SOFC applications. Reactivity tests with CGO found that the $x = 1.0$ sample showed a small reaction at 1000 °C/3 h, whereas the $x = 1.5$ and 2.0 did not. As with $YBaCo_{4-x}Zn_xO_7$, electronic conductivity was found to increase with temperature and decrease with increasing Zn content. The $x = 1.5$ material was the best compromise between phase stability and electronic conductivity. Symmetrical cells on CGO of this material were tested and as with $YBaCo_3ZnO_7$, it was found that the polarisation resistance could be improved by use of a 50:50 wt% composite cathode of the Td-Co material and CGO. In this study, Kim and Manthiram did not manufacture test cells with the composite $InBaCo_{2.5}Zn_{1.5}O_7$+CGO cathode material, so comparisons to those manufactured from $YBaCo_3ZnO_7$+CGO cannot be made. Analysis of their polarisation resistance data obtained from the symmetrical cells does indicate, however, that the Y Td-Co compound has a lower R_p than the In Td-Co compound, indicating that

$YBaCo_3ZnO_7$+CGO may be the better cathode material. Perhaps it was this realisation that encouraged Kim and Manthiram not to proceed with test cell manufacture for the In Td-Co compound.

Recently, Kim and Manthiram [187] have studied $Y_{1-x}Ca_xBaCo_{4-y}Zn_yO_7$. A large number of compounds in this solid solution were screened for thermal stability. Increasing the zinc content was found to improve the stability, whereas increasing the calcium content greater than $x = 0.5$ leads to deterioration. $Y_{0.75}Ca_{0.25}BaCo_{2.5}Zn_{1.5}O_7$, $Y_{0.5}Ca_{0.5}BaCo_{2.5}Zn_{1.5}O_7$ and $Y_{0.5}Ca_{0.5}BaCo_{2.25}Zn_{1.75}O_7$ were found to be stable over the IT-SOFC range of 600–800 °C for 120 h. No reaction was found with CGO at 900 and 950 °C for 3 h. After careful optimisation, $Y_{0.5}Ca_{0.5}BaCo_{2.5}Zn_{1.5}O_7$ was found to have good electrochemical performance and tested as an IT-SOFC cathode. Based on their previous work, Kim and Manthiram used a 50:50 wt% composite of $Y_{0.5}Ca_{0.5}BaCo_{2.5}Zn_{1.5}O_7$:CGO as a cathode for an anode-supported $Y_{0.5}Ca_{0.5}BaCo_{2.5}Zn_{1.5}O_7$+CGO|CGO|CGO+Ni (dense)|CGO+Ni(porous) test cell. The dense Ni+CGO layer provides better contact between the porous anode and dense electrolyte. A maximum power density of 451 mW cm^{-2} at 700 °C was found inferior performance to the $YBaCo_3ZnO_7$+CGO cathode material (520 at 700 °C) [185].

Vert et al. [188] have further extended the range of Td-Co compounds studied for SOFC applications; $RBaCo_3ZnO_7$ (R = Y, Er, Tb) were synthesised and studied as symmetrical cells on CGO. Electrode performance was found to increase (i.e., polarisation resistance was found to decrease) from Tb > Y > Er, which is interesting as it follows the radii trend for the trivalent Oh-coordinated ions; Tb (0.92 Å) > Y (0.90 Å) > Er (0.89 Å). Lattice parameter data, however, did indicate the possible presence of some Tb^{4+}. The lowest R_p value found was 35 mΩ cm^2 at 850 °C for $TbBaCo_3ZnO_7$. Given that Kim and Manthiram [184–186] consistently found that forming a composite cathode with 50 wt% CGO improved performance of the Td-Co compound, it would be an obvious next step to attempt this for $TbBaCo_3ZnO_7$. It would also be interesting to see if the trend of an increased lattice parameter leading to increased electrode performance was continued by extending the range of metal used to include slightly larger ions, for example, samarium and europium to form (Sm,Eu)$BaCo_3ZnO_7$. Composite cathodes of these with CGO should also be tested as this would be expected to result in improvements.

BIMEVOX-based composites

Bismuth-based oxides belonging to the Aurivillius family of phases are known to show good oxide-ion conductivity at IT-SOFC relevant temperatures, particularly those based on $Bi_4V_2O_{11}$ known as BIMEVOXs [189]. Their electronic conductivity is insufficient; so for potential cathode applications, they have been studied as composites with an electronically conducting metal.

In 2002, Xia and Liu presented work on a composite of BICUVOX.10 and 57 wt% Ag which showed some very promising results [190]. Anode-supported Ni+CGO|CGO|BICUVOX.10+Ag test cells were studied by AC impedance spectroscopy, and low values for the cathode-electrolyte interfacial resistance were found; 0.53 Ω cm^2 at 500 °C and 0.21 Ω cm^2 at 550 °C. These compare very well to values for typical perovskite cathodes, for example, LSCF–CGO (~10 Ω cm^2/500 °C) and SSC–CGO (~1 Ω cm^2/500 °C). Power densities for the BICUVOX.10+Ag cathode were also promising; 231 mW cm^{-2}/500 °C and 443 mW cm^{-2}/550 °C. At the time these were claimed to be the highest values in the literature for SOFCs operating at such low temperatures. Xia does comment, however, that the long-term stability of the cathode has yet to be characterised. The results have had a relatively minor impact on the wider community; the fact that the bismuth Aurivillius phases can lack thermal stability could mean that the BICUVOX.10+Ag composite lacks sufficient stability for commercial SOFC use.

Recently, Yang et al. [191] presented some work involving interesting techniques on a gold+BIMEVOX composite. Stimulated by the work of Xia and Liu, they attempted to improve the electronic conductivity of BICUVOX.10 using a metal element, this time gold. Rather than simply mechanically mixing the constituents of the composite, Yang et al. were able to deposit Au nanoparticles onto the surface of the BICUVOX.10 powder particles by a novel technique. The BICUVOX.10 was dispersed in a solution of $AuCl_4$ that was slowly reduced by dropwise addition of 0.5-M $NaBH_4$ solution. After washing and drying, gold particles of average diameter 10 nm were found to be evenly coated on the surface of the BICUVOX.10; the composite was denoted 'Au@BICUVOX.10'. An anode-supported test cell, Ni+CGO|CGO|Au@BICUVOX.10, was manufactured using another interesting technique; a pore-making carbon powder was used when applying the electrolyte to form finger-like microstructures that extended into the composite cathode, the aim being to extend the TPB lengths. Earlier tests with mechanically mixed Au+BICUVOX.10 indicated that 50 wt% gold was the optimum composition with regard to electronic conductivity and TEC-matching. The Au@BICUVOX.10 used in the test cell was 47 wt% Au. The author assumes that the solution method of synthesising Au@BICUVOX.10 makes achieving a precise wt% value impractical and that 47 wt%, once synthesised, was considered 'close enough' to 50 wt%. Maximum power densities for the test cell were 206 and 469 mW cm^{-2} at 500 and 550 °C, respectively. It was found that the Au@BICUVOX.10 cathode gave power

densities of about 90 mW cm^{-2} higher than mechanically mixed Au+BICUVOX.10. Stability tests found its power output to be 95% of the original after 20 h of operation.

The power density of the Au@BICUVOX.10 test cell at 550 °C is a slight improvement of 26 mW cm^{-2} over Xia and Liu's Ag+BICUVOX.10 cathode [190]. It would be interesting to see if the solution method for depositing nanoparticles could be employed for silver to manufacture Ag@BICUVOX.10. If similar improvements were seen over Ag+BICUVOX.10, then Ag@BICUVOX.10 would be a superior cathode material to Au@BICUVOX.10.

Following their work on Ag+BICUVOX.10 composites, Xia and Liu studied further composites based on silver and bismuth oxide materials known to have strong ionic conductivity [192]. Their cathode material was Ag+YSB (yttria-stabilised bismuth oxide, $Y_{0.25}Bi_{0.75}O_{1.5}$) formed from a 60:40 wt% mix of Ag_2O:YSB. ASR values were obtained for this cathode on a honeycomb-YSZ electrolyte and excellent results were initially found; 0.3 Ω cm^2 at 600 °C, which compares very well to common electrolyte/cathode interfacial resistances. As with their work on Ag+BICOVOX.10, Xia and Liu include at the end of their promising findings the caveat that the long-term stability of the composite cathode has yet to be studied. Subsequent work by Camaratta and Wachsman [193, 194] found that such stability is lacking. They tested symmetrical cells of Ag+YSB and Ag+ESB (erbium-stabilised bismuth oxide, $Er_{0.2}Bi_{0.8}O_{1.5}$), volume ratio of Ag:bismuth oxide = 60:40, using the respective pure bismuth oxide as the electrolyte (i.e., Ag+YSB|YSB|Ag+YSB and Ag+ESB|ESB|Ag+ESB). Initial ASRs were very low; 0.04 Ω cm^2 and 0.06 Ω cm^2 for Ag+YSB and Ag+ESB, respectively at 650 °C. However, after 100 h of operation at this temperature, these values were found to increase by approximately 70% [193]. XRD showed no evidence of reaction between the constituents of the composite; however, SEM revealed significant changes to the silver phase microstructure. A reduction in porosity is observed inhibiting gas transport leading to the reduced performance. Efforts were made to reduce the silver migration and densification [194]. Firstly, nano-sized 8YSZ powder was added, their theory being that this would lead to increased surface area thus increasing the energy required for the silver to migrate. Ag+($ESB_{1-x}YSZ_x$) $x = 0$, 0.05, 0.10, 0.15 by vol. frac. cathodes were tested and improvement was seen. The strongest improvement was for $x = 0.05$, which had a 95% reduced ASR degradation rate as well as an improved initial ASR of 0.043 Ω cm^2 at 650 °C. A second approach to improvement involved reducing the particle size of the initial ESB powder, the theory being the same as for adding nano-8YSZ with the advantage of being a more cost-effective method. After 7 days of vibratory milling, ESB particle size was reduced from the order of several microns to several hundred nanometres. As with the 8YSZ doping, this resulted in a dramatic reduction in the ASR degradation rate of 95% and a reduction of the initial ASR to 0.046 Ω cm^2. Although these are promising results, it must be noted that they are for unbiased symmetrical cells. Milling the ESB was repeated and retested including a 250 mV external bias. Improvement in the degradation rate was seen; however, it was only 50% as opposed to 95% and further improvement is necessary if Ag+ESB is going to be used by SOFC developers.

Soon after Camaratta and Wachsman published their, work Li et al. [195] presented work optimising the composition of Ag+ESB composite cathodes. Various volume rations of Ag:ESB were tested for ESB20 ($Er_{0.2}Bi_{0.8}O_{1.5}$) and ESB30 ($Er_{0.3}Bi_{0.7}O_{1.5}$) as unbiased symmetrical cells on the scandia stabilised zirconia (ScSZ) electrolyte. They found that a 50:50 volume ratio of Ag:ESB30 gave the best results, with ASRs of 0.50, 0.23 and 0.16 Ω cm^2 at 650, 700 and 750 °C. These performance data are similar to Xia and Liu's Ag+YSB|YSZ ASR of 0.3 Ω cm^2 at 600 °C [192]. However, Camaratta [193] found much lower ASR values for Ag+ESB|ESB, 0.06 Ω cm^2 at 650 °C; the matching of the electrolyte to the cathode material being the likely reason for this improvement. In their conclusions, Li et al. comment that the long-term stability of their Ag+ESB30 cathode needs to be tested. Given the known problems of Ag+ESB composites' long-term stability, it seems likely that much further work will be required if Li's optimised 50:50 Ag+ESB30 composite is to be used.

Other structure types

In 2007, Ehora et al. [196] studied $Ba_2Co_9O_{14}$. Although they were primarily interested in the low-temperature magnetic properties of this compound, they noted that its properties may make it desirable as an SOFC material; it has mixed-valence Co^{2+}/Co^{3+} that should allow for reasonable electronic conductivity at elevated temperature, and also TGA data suggest that oxygen vacancies form between 300 and 800 °C that could allow for ionic conductivity at these SOFC-relevant temperatures. Hence, Rolle et al. [197] have recently presented data on $Ba_2Co_9O_{14}$ as an IT-SOFC cathode material. Given the high cobalt content of this material and the octahedral coordination of this, it is not surprising that the TEC is prohibitively high; 20×10^{-6} K^{-1}, c.f. $\sim 10 \times 10^{-6}$ K^{-1} for CGO. Chemical compatibility between $Ba_2Co_9O_{14}$ and CGO and YSZ was shown hence composites, 70:30 wt.% $Ba_2Co_9O_{14}$+YSZ/CGO, were employed to reduce the TEC to acceptable levels. Symmetrical cells of $Ba_2Co_9O_{14}$+YSZ|YSZ|$Ba_2Co_9O_{14}$+YSZ and $Ba_2Co_9O_{14}$+CGO|CGO|-$Ba_2Co_9O_{14}$+CGO were tested. The best results were for the CGO case with a minimum ASR of 0.5 Ω cm^2 at

750 °C. This value is higher than that for one of the current 'best in class' cathodes; 70:30 wt% LSCF+CGO on CGO at 0.22 Ω cm^2 at 600 °C and 0.036 Ω cm^2 at 700 °C [198]. Further attempts could be made to improve $Ba_2Co_9O_{14}$ as a cathode material; the ratio of the composite could be varied and the cobalt content could be reduced by attempting substitutions for another transition metal element. Analogous to LSCF, attempting to synthesise solid solutions of $Ba_2Co_{9-x}Fe_xO_{14}$ would be a sensible starting point.

As an alternative structure type, work has been presented using the rutile-structured compound $Ir_{0.5}Mn_{0.5}O_2$ as a cathode material [199]. It was found to be chemically compatible with the LSGM electrolyte at 1000 °C. Tests on an $Ir_{0.5}Mn_{0.5}O_2$|LSGM|$Ir_{0.5}Mn_{0.5}O_2$ symmetrical cell found a minimum ASR value of 0.67 Ω cm^2 at 800 °C. However, tests on a single cell of $Ir_{0.5}Mn_{0.5}O_2$|LSGM|Pt found maximum power densities of 43.2 and 80.7 mW cm^{-2} at 600 and 800 °C, respectively.

Regarding the spinel-structured materials, the compound $Mn_{1.5}Co_{1.5}O_4$ (MCO) has been tested as a cathode material [200]. This was stimulated by the fact that MCO finds uses as a protection layer on the stainless steel interconnect of SOFCs and as such is known to have sufficient electronic conductivity and thermal stability under SOFC operating conditions. No reaction was found with YSZ after 3 h at 1100 °C. Tests on an anode-supported cell with a thin YSZ electrolyte were carried out firstly with a pure MCO cathode. A maximum power density of 386 mW cm^{-2} was found; insufficient for practical use. The reason for this was assigned to be the negligible ionic conductivity of MCO resulting in useful reactions only occurring at the TPB. In an attempt to improve on this, a 50:50 wt% MCO+SDC composite was tested that unexpectedly led to reduced performance of just 151 mW cm^{-2} at 800 °C. It was reasoned that the electronic conductivity of the composite was too low that led to difficulty with current collection. A current-collecting layer of SSC was coated on to the MCO+SDC composite and this led to improved power densities of 912 mW cm^{-2} at 800 °C. The power density at 650 °C, which is in the temperature region required for an IT-SOFC, was just 166 mW cm^{-2}, too low for practical applications. Attempts could be made to improve this by optimising the composite ratio and using a different electrolyte such as LSGM or CGO.

Some of these alternative SOFC cathode materials have shown great promise. ASR of some of the various compounds discussed is displayed in Fig. 8 along with data for the high-performance LSCF+CGO composite cathode of Wang et al. [198] for comparison. It is evident that the BICUVOX+Ag material shows a very low ASR with CGO at low temperatures [190]; however, it is commented that its long-term stability has yet to be characterised. Xia's YSB+Ag cathode also showed low ASRs with YSZ [192]; however, subsequent work by Camaratta and Wachsman [193, 194] has shown that stability is a problem with these compositions. The Td-Co compounds pioneered by Kim et al. [184–187] are an avenue of research with great potential; good performance has already been demonstrated and there are many compositional degrees of freedom that can be explored to improve on these further. The current best cathode in this family is a $YBaCo_3ZnO_7$+CGO composite. From the results of other encouraging non-perovskite cathodes, it is evident that the long-term stability of any new materials must be studied.

Mixed ionic-electronic conductors for solid oxide electrolysis cells (SOECs)

The inspiration for SOEC (Fig. 1) anode and cathode materials often comes from successful SOFC cathode and anode materials, respectively. However, the inlet atmosphere of a SOEC cathode contains much more steam than the outlet of a SOFC anode, and H_2 is required in the feed gas to prevent the oxidation of the common SOEC cathode material Ni-YSZ to NiO. An SOEC anode produces oxygen that can be directly collected or swept with air to minimise polarization. The atmospheres may have consequences on the stability and durability of the electrode materials chosen [201], and so a fuel cell cannot simply be reversed if efficient electrolysis cell is required. The studies performed in evaluating the potential for SOFC components to be used in SOECs are analyzed in the next section.

SOEC hydrogen cathodes

For an SOEC system, water is supplied to the porous negative cathode where it migrates to the electrolyte surface and is dissociated into hydrogen and oxygen by an

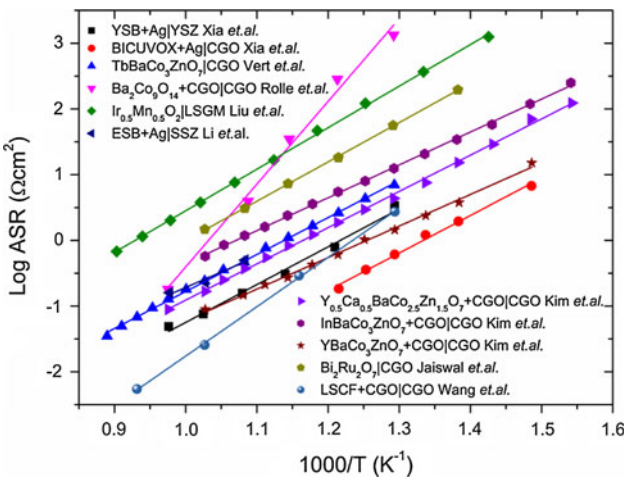

Fig. 8 Arrhenius plot of the polarization resistance on the interface electrolyte/electrode measured in air for different cathode systems

external supply of electrons. The hydrogen then travels back to the cathode surface, whereas the oxygen ions are transported through the solid electrolyte membrane to the anode. Oxygen partial pressures at this electrode can be of the order of 10^{-12}–10^{-16} bar [202]. The material must therefore be porous to allow transport of the reactant gas to the reactant sites and allow hydrogen to migrate to the electrode surface. As with fuel cell anodes, electrolysis cathodes tend to be a Ni-YSZ cermet, the metal conducts electrons, and mixing it with an ionic conductor such as YSZ increases the triple-phase boundary points. However, the gas inlet to a Ni-YSZ cathode must include ~5–10% mole fraction hydrogen to prevent the oxidation of the material to NiO [203, 204], which is less conductive and could lead to mechanical instability. Ideally, a material that is not easily oxidised is desired. Eguchi et al. [205] tested materials in both fuel cell and electrolysis modes. The materials studied were hydrogen cathodes Ni-YSZ and Pt; electrolytes $(ZrO_2)_{0.85}(YO_{1.5})_{0.15}$ and $(CeO_2)_{0.8}(SmO_{1.5})_{0.2}$ (YSZ and SDC, respectively); and oxygen electrodes $La_{0.6}Sr_{0.4}MnO_3$ and $La_{0.6}Sr_{0.4}CoO_3$ (LSM and LSC, respectively). It was found that the combination Ni-YSZ/YSZ/LSM was the best combination for fuel cell use and Pt/YSZ/LSC was the worst. In electrolysis mode however, the reverse was true. The low activity of Ni-YSZ in electrolysis mode is ascribed to Ni particles oxidised in the steam concentration, forming a less active layer. It is also found that the nickel particles in a Ni/YSZ composite coarsen in high-steam atmospheres or partially evaporate [206]. Osada et al. [207] tested the ionic conductor $(CeO_2)_{0.8}(SmO_{1.5})_{0.2}$ (CSO) with Ni as a cermet as an electrolysis cathode material in conjunction with a 0.5-mm thick ScSZ electrolyte and LSC anode. On both sides, a thin (~1 μm) CSO interlayer was deposited between the electrolyte and electrode to reduce contact resistance and reduce reactions between LSC and electrolyte. It was found that a loading of 17% vol. Ni-CSO was optimal for electrolysis use. Anymore and agglomeration of Ni particles is more likely. It was noted that the use of a highly ionically conductive electrolyte improved the performance of the cathode, but not the anode. The authors state that they achieved good performance of IR-free cell voltage = 1.13 V at 0.50 A cm^{-2} at 900 °C under the atmosphere of $H_2O + H_2$ ($p[H_2O] = 0.6$ atm) and O_2 (1 atm). However, it was conceded that at lower temperatures, their cell performed worse than optimised Ni-YSZ based cells from literature and so further research was required.

Marina et al. [206] compared Ni-YSZ with a titanate/ceria negative electrode $La_{0.35}Sr_{0.65}TiO_3$–$Ce_{0.5}La_{0.5}O_{2-\delta}$ in both electrolysis and fuel cell modes. When operated in fuel cell mode with a feed gas of 50:50 H_2O:H_2, the materials displayed the same order of resistance, i.e., at 800 °C at a constant polarization loss of 50 mV Ni-YSZ had an ASR of 0.26 Ω cm^2, whereas the composite was 0.29 Ω cm^2. However, under these conditions, but in electrolysis mode, the composite performed better, with the composite displaying ASR of 0.21 Ω cm^2 and Ni-YSZ 0.29 Ω cm^2. Varying pH_2O had more of an effect on the materials in electrolysis mode than in fuel cell mode. At a constant electrolysis, polarization loss of 0.1 V at 800 °C and partial pressure of H_2O varied from 0.5 to 0.9 atm, Ni-YSZ decreased from 0.56 to 0.4 Ω cm^2 and the composite decreased from 0.28 to 0.2 Ω cm^2.

Yang et al. [204] tested the perovskite $(La_{0.75}Sr_{0.25})_{0.95}Mn_{0.5}Cr_{0.5}O_3$ (LSCM) with YSZ and CGO as composite electrolysis cathode materials. The electrolyte used was YSZ and the anode was an LSM/YSZ composite. It was found that LSCM–CGO and LSCM–YSZ composites perform better than Ni–YSZ as electrolysis cathodes with or without the presence of H_2 in the feed gas and at all potentials. When the cathode feed gas is 3% steam/4% H_2/Ar, the LSCM composites display polarisation resistances of the order of 1 Ω cm^2 compared with around 10 Ω cm^2 for the Ni–YSZ cathode, although it is conceded that this is not representative of best literature Ni–YSZ values. When the potential is more negative, at about −0.2 V for LSCM/YSZ and −0.4 V for LSCM/CGO in an H_2-free atmosphere, polarisation resistance drastically increases. At further polarization at around −1.7 V, resistance decreases once again. A number of possible reasons for the diversion from ohmic behaviour are suggested. A reduction of LSCM at around −0.3 V is postulated, which can change the volume by 1%, decreasing conductivity. When at further negative potentials, it is hypothesised that the material may decompose into MnO and a Ruddlesden–Popper phase thereby reducing resistivity; however, this is not verified in the study.

There are contradictory studies which show that there is only a small resistance difference between using the Ni–YSZ in fuel cell or electrolysis mode [208, 209]. For example, Laguna-Bercero et al. [209] found comparable Ni–YSZ polarization potentials of 0.40 and 0.29 Ω cm^2 when run in electrolysis (+0.61 V) and fuel cell (−0.39 V) modes, respectively. The reason for the disagreement in the literature is not explained. However, it is noted that the role of microstructure on electrochemical performance is not fully understood for the electrolysis cathode.

Oxygen anode

At an SOEC anode surface, the electrochemically delivered oxygen ions are oxidised to become oxygen molecules. As with the cathode, a mixed ionic and electronic conducting material is required with a similar thermal expansion coefficient as the electrolyte. Most commonly, perovskites are used for SOEC anodes. A lot of the work in finding suitable SOEC anodes has centred on testing known

successful SOFC cathodes, for example, the perovskite Sr-doped lanthanum manganite $LaMnO_3$ is a popular SOFC cathode because of its high electrical conductivity, stability and compatibility with common electrolytes [210]. Doping Sr^{2+} on the La^{3+} site can improve conductivity as Mn^{4+} is increased, but has the disadvantage of increasing the thermal expansion coefficient [211] and not being ionically conductive as well as electronically conductive [212]. There is also risk of MnO_x migrating from the LSM phase into the YSZ, allowing the La_2O_3 or SrO to react with YSZ to form less conductive $La_2Zr_2O_7$ or $SrZrO_3$ [202, 213–215]. Overdoping the LSM with MnO_x by just a small percent ensures there is no free La_2O_3 or SrO to react with the YSZ [202]. Laguna-Bercero et al. [216] detected evidence of $La_2Zr_2O_7$ when $La_{0.6}Sr_{0.4}Co_{0.2}Fe_{0.8}O_{3-\delta}$ (LSCF) or $La_{0.8}Sr_{0.2}MnO_{3-\delta}$–YSZ (LSM-YSZ) composites were used as an electrode in contact with 1% Ce-substituted Scandia Stabilised Zirconia (10Sc1CeSZ) but found it to have no adverse effect on performance giving ASR values 0.93 Ω cm^2 for the LSM cell and 0.79 Ω cm^2 for the LSCF cell at 800 °C under electrolysis mode with 70% H_2O supplied to the Ni–YSZ electrode. It should be noted that these materials performed better in fuel cell mode under the same conditions. It was also found that the LSM–YSZ composite on ScCeSZ showed degradation after use; this is attributed to a distortion to rhombohedral β-$Sc_2Zr_7O_{17}$ phase.

Wang et al. [214] eliminated the formation of the insulating layers of these materials by synthesising composites of YSZ with $La_{0.8}Sr_{0.2}CoO_3$ (LSCo), $La_{0.8}Sr_{0.2}FeO_3$ (LSF) and $La_{0.8}Sr_{0.2}MnO_3$ (LSM), respectively. It was found that LSM–YSZ is a less than ideal electrode material, despite an initial improvement of impedance when run in fuel cell mode as performance decreased during electrolysis mode. The LSC–YSZ and LSF–YSZ composites showed good initial performance with no need for a preliminary cathode polarization step. The LSC–YSZ anode showed the best initial performance of the three, but was noted to deactivate after time in electrolysis mode. The LSF–YSZ anode on the other hand was proven to be stable during electrolysis over a period of 100 h. [214] Directly after fuel cell polarization (570 mA cm^{-2}), the LSM–YSZ anode displayed, at OCV, a total cell impedance of 1.8 Ω cm^2 but after 180 min in electrolysis mode (285 mA cm^{-2}), the electrode impedance had increased to about 4 Ω cm^2. It is explained that under oxidising conditions, LSM distributes forming an LSM film preventing the diffusion of oxygen ions. This is temporarily reversed if run in fuel cell mode.

Conversely, Marina et al. [206] found LSM to be a reversible oxygen material when they studied $La_{0.8}Sr_{0.2}FeO_{3-\delta}$ (LSF), $La_{0.7}Sr_{0.3}Cu_{0.1}Fe_{0.9}O_{3-\delta}$ (LSCuF), $La_{0.6}Sr_{0.4}Co_{0.2}Fe_{0.8}O_{3-\delta}$ (LSCF) and $La_{0.8}Sr_{0.2}MnO_{3-\delta}$ (LSM) as oxygen electrodes in reversible cells. In all cases, the materials performed better in fuel cell mode than in electrolysis mode. Of these, four materials LSF and LSM showed the most reversibility, having similar overpotentials in fuel cell and electrolysis modes. LSCuF and LSCF were notably better in fuel cell mode than electrolysis.

Kuharuangrong [211] tested the effect of doping LSM with Ni on the Mn site. It is explained that increasing the Sr^{2+} content in LSM increases electrical conductivity by increasing the concentration of Mn^{4+}; however, the compromise is an increase in TEC that results in a mismatch with other common materials. It was found that doping and increasing the amount of Ni^{2+} on the Mn side decreased the Mn^{3+} concentration, decreasing electrical conductivity at 900 °C from 107 S cm^{-1} for undoped LSM to 48 S cm^{-1} for LSM doped with 30-mole% Ni.

Yu et al. [217] investigated a $Ba_{0.5}Sr_{0.5}Co_{0.8}Fe_{0.2}O_{3-\delta}$ (BSCF) oxygen anode with a YSZ electrolyte and Ni–YSZ hydrogen cathode, finding that electrode ASR values of 0.66 Ω cm^2 at 750 °C, 0.27 Ω cm^2 at 800 °C and 0.077 Ω cm^2 at 850 °C were produced. Yu et al. claim this material performs better than common SOEC anode materials, e.g., LSC, LSF and LSM, but the ASRs reported are similar to those of other authors discussed above. However, when operated in electrolysis mode, the BSCF/YSZ/Ni–YSZ cell H_2 output, 147.2 mL cm^{-2} h^{-1} of hydrogen, was almost three times the amount produced by a more conventional LSM/YSZ/Ni–YSZ cell that produced just 49.8 mL cm^{-2} h^{-1}.

As Laguna-Bercero et al. [209] suggest that $La_2NiO_{4+\delta}$ (LNO) type materials should be studied for use as oxygen electrodes, the lanthanide nickelates, the family of composition Ln_2NiO_4 (Ln = La, Nd, Pr), are increasingly studied as oxygen electrode materials. This is mostly because of the high oxygen transport values and wide range of oxygen stoichiometries that are possible as a function of the oxygen partial pressure [218]. LNO is able to accommodate excess oxygen under high pO_2 through interstitials and can also cope with low pO_2 atmospheres through oxygen loss [210]. For instance, higher electrical conductivities and oxygen interstitial concentrations have been reported for $La_2Ni_{0.6}Cu_{0.4}O_{4+\delta}$ after heat treatments under high oxygen pressure [219]. Along with high oxygen ion transportation, another advantage of LNO is its low lattice expansion in changing temperatures and oxygen partial pressures [220]. However, it is not recommended that this material be used in conjunction with the electrolyte YSZ as interfacial reactions between the electrode and electrolyte have been inferred, forming the insulating $La_2Zr_2O_7$ phase [210, 221]. Rieu et al. [221] tested graded LNO electrode layers on YSZ that included a CGO diffusion barrier, a dense thin LNO layer and a thick porous LNO layer. It was found that the porous LNO layer readily delaminated from the CGO interlayer but the addition of the dense thin LNO

layer improved adhesion and provided more contact points for oxygen diffusion to the electrolyte. Using this setup, an ASR of 0.11 Ω cm^2 was achieved for a symmetrical cell with Pt current collectors at 800 °C. It should be noted that a Pt current collector can only be used up to temperatures of around 700–800 °C as greater than this temperature Pt is thought to catalyze the irreversible formation of higher order Ruddlesden–Popper phases, $La_3Ni_2O_{7-\delta}$ and $La_4Ni_3O_{10-\delta}$ caused by the oxidation of LNO [222].

Some lanthanum nickelate–based materials also perform more effectively in electrolysis, rather than fuel cell mode. Perez-Coll et al. [223] tested La_2NiO_4, $La_3Ni_2O_7$ and a La_2NiO_4–$Ce_{0.8}Sm_{0.2}O_{2-\delta}$ composites as electrodes in symmetrical cells on $Ce_{0.8}Sm_{0.2}O_{2-\delta}$ + 2%Co electrolyte. Applying a cathodic, fuel cell polarization of 530 mA cm^{-2} improved the electrode polarization resistance from 3.30 Ω cm^2 at OCV to 0.32 Ω cm^2 at 700 °C. The effect of applying an anodic current was even more pronounced. This trend was observed for all the lanthanum nickelate materials tested, though less significant for the composite. The addition of the ionically conductive CSO material significantly improved electrode performance. Applying a cathodic polarization of 530 mA cm^{-2} improved the composite electrode polarization resistance from 0.64 Ω cm^2 at OCV to 0.34 Ω cm^2 at 700 °C.

An example of doping on the A (La) site of LNO is the addition of up to 0.3 Sr^{2+} in place of La^{3+} that reportedly reduces electrical resistance and improves stability [224]. However, it is noted elsewhere [213] that the addition of Sr increases oxygen vacancies when doped into perovskite materials, and so reduces ionic conductivity in K_2NiF_4 structures because these materials conduct oxygen predominantly through interstitials. Aguadero et al. [224] agree that Sr^{2+} doping in place of La^{3+} decreases ionic conductivity because of the hole-doping effect resulting in the oxidation of Ni^{2+} to Ni^{3+} to preserve charge neutrality without the need of excess oxygen. It is argued that the reduction of ionic conduction is acceptable for the increase of electronic conductivity that is noted to be poor in LNO. It was also found that ionic and electronic conductivity of $La_{1.9}Sr_{0.1}NiO_{4+\delta}$ could be increased by applying heat treatment of 650 °C and high oxygen pressure of 200 bar to the powders; this treatment increases electrical conductivity and oxygen interstitial concentration [224]. It is noted that the temperatures used should not be so high as to form unwanted higher-order Ruddlesden–Popper phases ($La_{n+1}Ni_nO_{3n+1}$) [225].

Epitaxial thin film electrodes

Several studies have been performed using nearly fully dense polycrystalline, even ideally single crystals or epitaxial films to avoid the effects of microstructure and composition in the comprehension of the intrinsic properties of the materials as previously commented by Adler [226] and reported in several comprehensive review articles about thin film technologies for SOFCs [227–230].

Ruddlesden–Popper (RP)-type oxides have attracted great interest as epitaxial thin films because of their intrinsic anisotropic transport properties. Before a fuel cell application can be considered for these thin film RP oxides, many of the fundamental parameters governing fuel cell performance have to be determined. Evidently, these may differ significantly from the bulk materials. Kim et al. [231] first successfully deposited the (100)-oriented epitaxial films of $La_2NiO_{4+\delta}$ on $LaAlO_3$ (001) substrates by pulsed laser deposition (PLD). The authors determined the oxygen transport behaviour on a 300-nm thick film using electrical conductivity relaxation (ECR) measurements and suggest that the performance is controlled by the surface exchange reaction. In a subsequent article [232], using AC impedance spectroscopy, the authors investigated the kinetic behaviour of dense polycrystalline La_2NiO_4 thin films with a thickness of 300 nm, grown on yttrium-stabilized zirconia (YSZ) single-crystal substrates by PLD. Furthermore, very high-quality epitaxial La_2NiO_4 films grown along *c*-axis direction on single-crystal $SrTiO_3$ (STO) (100) and $NdGaO_3$ (NGO) (110) substrates were attained by Garcia et al. [233] through the use of pulsed injection metal organic chemical vapour deposition (PI-MOCVD). The authors observed that the values of the electrical conductivity improved significantly with decreasing film thickness such that the values are prominently superior to the highest from bulk materials (~100 S cm^{-1}) [164, 234], and even the values from layers of 50 nm and thinner films are strikingly higher than those from single crystals along the *ab*-axis (~200 S cm^{-1}) [160, 235]. Subsequently, a maximum value for the electrical conductivity of this material (475 S cm^{-1}) in 33-nm thick films was reported by Burriel et al. [236]. They also comment that the absolute strain plays a key role in the transport properties of this material. Further works regarding determining the anisotropic tracer diffusion and surface exchange coefficients of the epitaxial La_2NiO_4 films by oxygen isotopic exchange and distribution through the isotope exchange depth profile (IEDP) method were performed. The authors developed a new and effective method for the measurements of transport properties in two directions, traverse and longitudinal, as shown in Fig. 9 [167]. Both tracer diffusion coefficients along the *c*-direction and *ab*-direction tend to increase with increasing thickness. It, however, seems that both surface exchange coefficients along the two different directions have no direct correlation with film thickness. This study corroborated that the oxygen diffusion and surface exchange exhibits highly anisotropic behaviour and both give data 2–3 orders of magnitude higher along the *ab*-

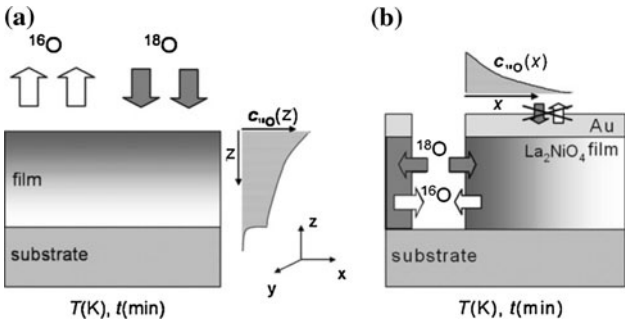

Fig. 9 Schematic diagrams of sample configuration for (**a**) traverse and (**b**) longitudinal oxygen tracer transport measurements (adapted from Ref. [167])

plane than those along the *c*-direction. Figures 10 and 11 show a comparison of oxygen diffusion and surface exchange coefficients (D^* and k^*, respectively) from dense polycrystalline, single-crystal and epitaxial $La_2NiO_{4+\delta}$ thin film samples [167].

Higher-order RP-phase lanthanum nickel oxide films ($n = 2$ and 3) have been only demonstrated by Raju et al. [237]. In their studies, oriented perovskite-type $LaNiO_3$, K_2NiF_4-type La_2NiO_4 and higher-order RP-phase $La_3Ni_2O_7$ and $La_4Ni_3O_{10}$ films have been synthesised through the method of nebulized spray pyrolysis with a low-processing temperature and the use of precursors of lanthanum and nickel acetylacetonate mixture. Even though the cation stoichiometry of $La_3Ni_2O_7$ and $La_4Ni_3O_{10}$ vary from the ideal values and there is some doubt whether the higher-order RP films are oriented, the research is the only report of depositing the $n = 2$ and 3 members of the monophasic RP-type films. More recently, Burriel et al. [238] attempted

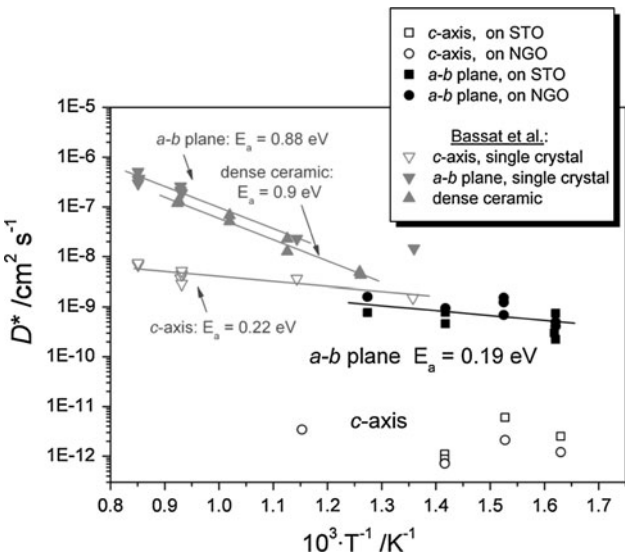

Fig. 10 Anisotropy of diffusion for La_2NiO_4 films deposited on STO and on NGO in comparison with the literature data for La_2NiO_4 single crystal and dense ceramics [167]

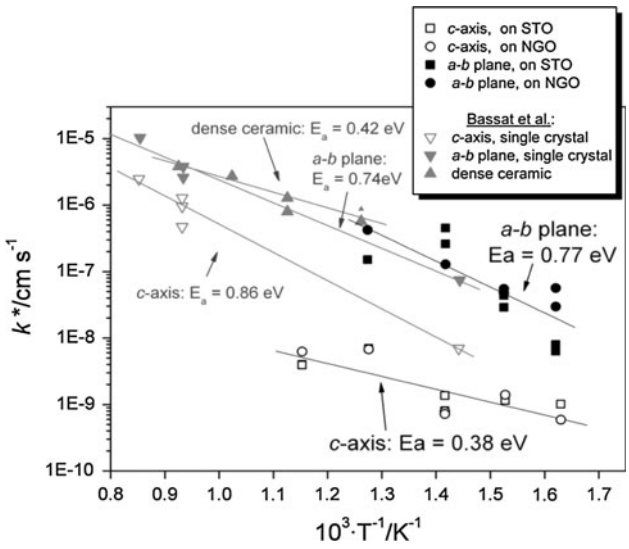

Fig. 11 Anisotropy of surface exchange property for La_2NiO_4 films deposited on STO and on NGO in comparison with the literature data for La_2NiO_4 single crystal and dense ceramics [167]

to deposit the pure $La_3Ni_2O_7$ and $La_4Ni_3O_{10}$ thin films by PI-MOCVD. However, despite mixed-phase films being obtained, particular films composed of pure La_2NiO_4 and $LaNiO_3$ forming a microstructure with disordered intermixed nanodomains were observed. These nanodomains progressively increased with the *n* value, and the electronic conductivity also shows a progressive change from the semiconducting to metallic behaviour, meaning the transport properties in nanostructured epitaxial films of the $La_{n+1}Ni_nO_{3n+1}$ series could be enhanced by the nanodomains, as commented by the authors. This suggests a new research direction in the preparation of nanocomposite films with tailored properties.

Of further interest are heterostructured thin film oxides for SOFCs building on the earlier interest in strain at interfaces and the natural layered nature of the RP-phase oxide films. RP-phases possess natural heterostructures with alternating blocks of perovskite and rock-salt. Thus, it is of interest to investigate whether growing heteroepitaxial films of these oxides will enhance electrical and electrochemical properties in SOFC cathodes in comparison with the individual bulk materials. For example, an enhancement of oxygen surface exchange on the hetero-interface of (La, Sr)CoO_3/(La, Sr)$_2CoO_4$ polycrystalline layered-films has been reported by Sase et al. [239]. Further evidence is presented by oxygen reduction kinetics enhancement on heterostructured interfaces of $La_{0.8}Sr_{0.2}CoO_{3-\delta}$ (LSC_{113})/$(La_{0.5}Sr_{0.5})_2CoO_{4\pm\delta}$ (LSC_{214}) epitaxial films demonstrated by Crumlin et al. [240]. For the first example of half cells with epitaxial films on epitaxial electrolyte substrates, Yamada et al. [241] deposited heteroepitaxial SOFC systems. The system is composed of 14-nm thick (110) RP-type $Nd_2NiO_{4+\delta}$ epitaxial films on (100) YSZ

single-crystal electrolytes. The authors claim that the type of K_2NiF_4 structure may possess a certain extent of inherent flexibility enabling epitaxial growth. They discovered $Nd_2NiO_{4+\delta}$ epitaxy can grow along the orientation of (110) plane on (100) YSZ substrates although its lattice mismatch is as large as that of 9.9% with the YSZ substrates. With the rather similar value of lattice mismatch along growing directions of (100) or (001), however, it is surprising that they found no other orientations (for instance, (100) or (001)) of $Nd_2NiO_{4+\delta}$ epitaxial films have been grown on the (100) YSZ substrates. This might be caused by the different surface energy of crystal planes. Furthermore, the authors also found the activation energy for oxide-ion conductivity in the series of epitaxial films is significantly influenced by orientation, presumably as a result of the strong compressive strain. This is the first example of the heteroepitaxial SOFC system to date. From this work, it is clear that the advantage of intrinsic oxygen anisotropic transport properties in RP-phase materials can be exploited, and offers the possibility of optimising their oxide-ionic transport by preparing highly oriented samples to align channels of oxide-ion diffusion.

Conclusions

The need to find novel materials with good performance in solid-state electrochemical devices such as SOFCs and SOECs at intermediate temperatures (500–700 °C) has promoted the study of a significant number of different materials. The study of the defect chemistry and physical properties relationships has increased the knowledge of the different factors governing the transport and mechanical properties of these cells and the effect of the performance of the different materials on the other cell components.

Gd-doped cerium oxide is considered one of the most effective materials for use as an IT-SOFC electrolyte because of its high ionic conductivity in the intermediate-temperature range and the possession of a thermal expansion coefficient comparable to that of stainless steel. It is, however, necessary to sinter CGO at a temperature that will not prove detrimental to any steel interconnect used in the cell. Considerable reduction in the sintering temperature of CGO through doping with small concentrations of transition metal oxides has been achieved. The effect of these additives on the grain and bulk ionic conductivity, and the possible mechanisms for the improvement on the densification, has also been reported. Regarding the development of mixed ionic-electronic conductors, several materials with perovskite-like structures have been studied. Among them Co-containing phases appear to present the higher values of oxygen conductivity and lower polarization resistances at intermediate temperatures. Promising alternative materials have been found particularly within the pyrochlore and $YBaCo_3ZnO_7$ derivatives, and so it is expected that further investigations would lead to the development of materials with improved properties for intermediate-temperature applications.

Although fuel cell electrode electrochemistry is relatively well understood, it seems that further research should be directed towards understanding the electrochemical reactions on the micro-scale and the importance of impurities on performance of the hydrogen cathode in SOECs. For SOEC anodes, the conventional lanthanum transition metal perovskites as $La_{0.8}Sr_{0.2}FeO_{3-\delta}$ (LSF), $La_{0.7}Sr_{0.3}Cu_{0.1}Fe_{0.9}O_{3-\delta}$ (LSCuF), $La_{0.6}Sr_{0.4}Co_{0.2}Fe_{0.8}O_{3-\delta}$ (LSCoF) and $La_{0.8}Sr_{0.2}MnO_{3-\delta}$ (LSM) were identified as functioning better in a fuel cell mode rather than electrolysis mode. However, $Ba_{0.5}Sr_{0.5}Co_{0.8}Fe_{0.2}O_{3-\delta}$ (BSCF) and some lanthanum nickelate–based materials from the Ruddlesden–Popper family perform more effectively in electrolysis, rather than fuel cell mode. Also, the study of these materials as epitaxial thin films highlights that the application of thin film techniques in SOFC and SOEC technologies could significantly improve the performance of anisotropic oxides and favour their implementation in intermediate-temperature devices.

References

1. Steele BCH, Heinzel A (2001) Nature 414:345
2. Matsuzaki Y, Yasuda I (2002) Solid State Ionics 152:463
3. Athanassiou C, Pekridis G, Kaklidis N, Kalimeri K, Vartzoka S, Marnellos G (2007) Int J Hydrogen Energ 32:38
4. Bastidas DM, Tao SW, Irvine JTS (2006) J Mater Chem 16:1603
5. Liu M, Yu B, Xu J, Chen J (2008) J Power Sources 177:493
6. Yu B, Zhang W, Chen J, Xu J, Wang S (2008) Sci China B Chem 51:289
7. Huang K, Wan J, Goodenough JB (2001) J Mater Sci 36:1093. doi:10.1023/A:1004813305237
8. Ralph JM, Schoeler AC, Krumpelt M (2001) J Mater Sci 36:1161. doi:10.1023/A:1004881825710
9. Steele BCH (2001) J Mater Sci 36:1053. doi:10.1023/A:1004853019349
10. Minh NQ (1993) J Am Ceram Soc 76:563
11. Badwal SPS (1992) Solid State Ionics 52:23
12. Etsell TH, Flengas SN (1970) Chem Rev 70:339
13. Steele BCH (2000) Solid State Ionics 129:95
14. Sammes NM, Tompsett GA, Nafe H, Aldinger F (1999) J Eur Ceram Soc 19:1801
15. Takahashi T, Iwahara H, Arao T (1975) J Appl Electrochem 5:187
16. Verkerk MJ, Keizer K, Burggraaf AJ (1980) J Appl Electrochem 10:81
17. Jacobson AJ (2010) Chem Mater 22:660
18. Ishihara T, Matsuda H, Takita Y (1994) J Am Chem Soc 116:3801
19. Huang PN, Petric A (1996) J Electrochem Soc 143:1644
20. Djurado E, Labeau M (1998) J Eur Ceram Soc 18:1397
21. Stevenson JW, Armstrong TR, Pederson LR, Li J, Lewinsohn CA, Baskaran S (1998) Solid State Ionics 113:571

22. Yamaji K, Horita T, Ishikawa M, Sakai N, Yokokawa H (1999) Solid State Ionics 121:217
23. Huang PN, Horky A, Petric A (1999) J Am Ceram Soc 82:2402
24. Kim KN, Kim BK, Son JW et al (2006) Solid State Ionics 177:2155
25. Lin YB, Barnett SA (2006) Electrochem Solid State Lett 9:A285
26. Bi Z, Dong Y, Cheng M, Yi B (2006) J Power Sources 161:34
27. Inaba H, Tagawa H (1996) Solid State Ionics 83:1
28. Inaba H, Nakajima T, Tagawa H (1998) Solid State Ionics 106:263
29. Rambabu B, Ghosh S, Jena H (2006) J Mater Sci 41:7530. doi:10.1007/s10853-006-0837-6
30. Esposito V, Zunic M, Traversa E (2009) Solid State Ionics 180:1069
31. Kleinlogel C, Gauckler LJ (2000) Solid State Ionics 135:567
32. Jud E, Gauckler LJ (2005) J Electroceram 14:247
33. Kleinlogel C, Gauckler LJ (2001) Adv Mater 13:1081
34. Lewis GS (2002) PhD Thesis, University of London
35. Jud E, Zhang Z, Sigle W, Gauckler LJ (2006) J Electroceram 16:191
36. Lewis GS, Atkinson A, Steele BCH, Drennan J (2002) Solid State Ionics 152:567
37. Fagg DP, Abrantes JCC, Perez-Coll D, Nunez P, Kharton VV, Frade JR (2003) Electrochim Acta 48:1023
38. Zhang ZL, Wilfried SA, Ruhle M, Jud E, Gauckler LJ (2007) Acta Mater 55:2907
39. Jud E, Huwiler CB, Gauckler LJ (2005) J Am Ceram Soc 88:3013
40. Kleinlogel CM, Gauckler LJ (2000) J Electroceram 5:231
41. Nicholas JD, De Jonghe LC (2007) Solid State Ionics 178:1187
42. Kim DJ (1989) J Am Ceram Soc 72:1415
43. Kleinlogel C, Gauckler LJ (1999) Electrochem Soc Proc 99-19:225
44. Avila-Paredes HJ, Kim S (2006) Solid State Ionics 177:3075
45. Zajac W, Suescun L, Swierczek K, Molenda J (2009) J Power Sources 194:2
46. Fagg DP, Kharton VV, Frade JR (2002) J Electroceram 9:199
47. Ou DR, Mori T, Ye F et al (2009) J Electrochem Soc 156:B825
48. Zhang TS, Kong LB, Zeng ZQ et al (2003) J Solid State Electrochem 7:348
49. Pikalova EY, Demina AN, Demin AK, Murashkina AA, Sopernikov VE, Esina NO (2007) Inorg Mater 43:735
50. Dong Q, ZH Du, Zhang TS, Lu J, Song XC, Ma J (2009) Int J Hydrogen Energ 34:7903
51. Zhang TS, Ma J, Kong LB, Chan SH, Hing P, Kilner JA (2004) Solid State Ionics 167:203
52. Kondakindi RR, Karan K (2009) Mater Chem Phys 115:728
53. Zhang TS, Ma J, Leng YJ, Chan SH, Hing P, Kilner JA (2004) Solid State Ionics 168:187
54. Figueiredo FM, Marques FMB, Frade JR (1998) Solid State Ionics 111:273
55. Petrov AN, Cherepanov VA, Zuev AY (2006) J Solid State Electrochem 10:517
56. Zuev AY, Petrov AN, Vylkov AI, Tsvetkov DS (2007) J Mater Sci 42:1901. doi:10.1007/s10853-006-0345-8
57. Seppaenen KM, Taskinen P (1980) Scand J Metallurgy 9:3
58. Mizusaki J, Mima Y, Yamauchi S, Fueki K, Tagawa H (1989) J Solid State Chem 80:102
59. Petrov AN, Cherepanov VA, Zuev AY (1987) Russ J Phys Chem A 61:630
60. Petrov AN, Zuev AY, Vylkov AI, Tsvetkov DS (2007) J Mater Sci 42:1909. doi:10.1007/s10853-006-0346-7
61. Zuev AY, Vylkov AI, Petrov AN, Tsvetkov DS (2008) Solid State Ionics 179:1876
62. Senarfs-Rodriguez MA, Goodenough JB (1995) J Solid State Chem 116:224
63. Thorntonf G, Owen IW, Diakun GP (1991) J Phys Conden Matter 3:417
64. Nakamura T, Misono M, Yoneda Y (1981) Chem Lett 10
65. Gavrilova LY, Cherepanov VA (1999) In: Singhal SC, Dokiya M (eds) Solid oxide fuel cells VI, PV 99-17. The Electrochemical Society Proceedings Series. The Electrochemical Society, Pennington, p 404
66. Cherepanov VA, Gavrilova LY, Petrov AN, Zuev AY (2002) Z Anorg Allge Chem 628:2140
67. Teraoka Y, Yoshimatsu M, Yamazoe N, Seiyama T (1984) Chem Lett 13:893
68. Søgaard M, Vang P, Mogensen M, Willy F, Skou E (2006) Structure 177:3285
69. Rudberg EA, Wiik K, Svensson AM, Nisancioglu K (2005) Solid State Electrochem 311
70. Bouwmeester HJM (2003) Catalysis Today 82:141
71. Matsuura T, Tabuchi J, Mizusaki J, Yamauchi S, Fueki K (1988) J Phys Chem Solids 49:1403
72. Lankhorst MHR, Bouwmeester HJM, Verweij H (1996) Phys Rev Lett 77:2989
73. Lankhorst MHR, Bouwmeester HJM, Verweij H (1997) Solid State Ionics 96:21
74. Lankhorst MHR, Bouwmeester HJM, Verweij H (1997) J Solid State Chem 133:555
75. Petrov AN, Kononchuk OF, Andreev AV, Cherepanov VA, Kofstad P (1995) Solid State Ionics 80:189
76. Patrakeev MV, Leonidov IA, Mitberg EB et al (1999) Ionics 5:444
77. Kozhevnikov VL, Leonidov IA, Mitberg EB, Patrakeev MV, Petrov AN, Poeppelmeier KR (2003) J Solid State Chem 172:296
78. Sehlin SR, Anderson HU, Sparlin DM (1995) Phys Rev B 52:11681
79. van Doorn RE, Fullarton IC, de Souza RA, Kilner JA, Bouwmeester HJM, Burggraaf AJ (1997) Solid State Ionics 96:1
80. Berenov AV, Atkinson A, Kilner JA, Bucher E, Sitte W (2010) Solid State Ionics 181:819
81. Bucher E, Sitte W, Rom I, Papst I, Grogger W, Hofer F (2002) Solid State Ionics 152–153:417
82. Yamamoto O, Takeda Y, Kanno R, Noda M (1987) Solid State Ionics 22:241
83. Tai LW, Nasrallah MM, Anderson HU, Sparlin DM, Sehlin SR (1995) Solid State Ionics 76:259
84. Maguirea E, Gharbage B, Marques FMB, Labrincha JA (2000) Solid State Ionics 127
85. Guntuka S, Banerjee S, Farooq S, Srinivasan MP (2008) Ind Eng Chem Res 47:154
86. Kharton VV, Kovalevsky AV, Tikhonovich VN, Naumovich EN, Viskup AP (1998) Solid State Ionics 110:53
87. Yaremchenko AA, Kharton VV, Viskup AP, Naumovich EN, Tikhonovich VN, Lapchuk NM (1999) Solid State Ionics 120:65
88. Sukpirom N, Iamsaard S, Charojrochkul S, Yeyongchaiwat J (2011) J Mater Sci 46:6500. doi:10.1007/s10853-011-5596-3
89. Hrovat M, Katsarakis N, Reichmann K, Bernik S, Kuscer D, Holc J (1996) Solid State Ionics 83:99
90. Chen CH, Kruidhof H, Bouwmeester HJM, Burggraaf AJ (1997) J Appl Electrochem 27:71
91. Kharton VV, Viskup AP, Bochkov DM, Naumovich EN, Reut OP (1998) Solid State Ionics 110:61
92. Junichiro M (1992) Solid State Ionics 52:79
93. Inoue T, Kamimae J-i, Ueda M, Eguchi K, Arai H (1993) J Mater Chem 3:751
94. Hjalmarsson P, Søgaard M, Hagen A, Mogensen M (2008) Solid State Ionics 179:636
95. Huang K, Lee HY, Goodenough JB (1998) J Electrochem Soc 145:3220. doi:10.1149/1.1838789

96. Tai LW, Nasrallah MM, Anderson HU, Sparlin DM, Sehlin SR (1995) Solid State Ionics 76:273
97. Tai LW, Nasrallah MM, Anderson HU (1995) J Solid State Chem 118:117
98. Skinner SJ, Kilner JA (2003) Materials Today 6:30
99. Stevenson JW, Armstrong TR, Carneim RD, Pederson LR, Weber WJ (1996) J Electrochem Soc 143:2722
100. Petric A, Huang P, Tietz F (2000) Solid State Ionics 135:719
101. Teraoka Y, Zhang HM, Okamoto K, Yamazoe N (1988) Mater Res Bull 23:51
102. Esquirol A, Kilner J, Brandon N (2004) Solid State Ionics 175:63
103. Wang S, Kato T, Nagata S et al (2002) Solid State Ionics 146:203
104. Wang S, Katsuki M, Dokiya M, Hashimoto T (2003) Solid State Ionics 159:71
105. Deng ZQ, Yang WS, Liu W, Chen CS (2006) J Solid State Chem 179:362
106. Takeda Y, Kanno R, Takada T, Yamamoto O, Takano M, Bando Y (1986) Z Anorg Allge Chem 541:259
107. de la Calle C, Aguadero A, Alonso JA, Fernandez-Diaz MT (2008) Solid State Sci 10:1924
108. Takeda T, Yamaguchi Y, Watanabe H, Tomiyoshi S, Yamamoto H (1969) J Phys Soc Jpn 26:1320
109. Grenier JC, Ghodbane S, Demazeau G, Pouchard M, Hagenmuller P (1979) Mater Res Bull 14:831
110. Battle PD, Gibb TC, Steel AT (1987) J Chem Soc-Dalton Trans 2359
111. Battle PD, Gibb TC (1987) J Chem Soc-Dalton Trans 667
112. Battle PD, Gibb TC, Steel AT (1988) J Chem Soc-Dalton Trans 83
113. Harrison WTA, Hegwood SL, Jacobson AJ (1995) J Chem Soc-Chem Commun 1953
114. Nagai T, Ito W, Sakon T (2007) Solid State Ionics 177:3433
115. Zeng P, Shao Z, Liu S, Xu ZP (2009) Separ Purif Techn 67:304
116. Zhou W, Jin W, Zhu Z, Shao Z (2010) Int J Hydrogen Energ 35:1356
117. Aguadero A, de la Calle C, Alonso JA, Escudero MJ, Fernandez-Diaz MT, Daza L (2007) Chem Mater 19:6437
118. Aguadero A, Perez-Coll D, de la Calle C, Alonso JA, Escudero MJ, Daza L (2009) J Power Sources 192:132
119. Aguadero A, Antonio Alonso J, Perez-Coll D, de la Calle C, Fernandez-Diaz MT, Goodenough JB (2010) Chem Mater 22:789
120. Shen Y, Wang F, Ma X, He T (2011) J Power Sources 196:7420
121. Zeng PY, Ran R, Shao ZP, Yu H, Liu SM (2009) Braz J Chem Eng 26:563
122. Zeng P, Ran R, Chen Z et al (2008) J Alloys Cmpnds 455:465
123. Chen X, Huang L, Wei Y, Wang H (2011) J Membr Sci 368:159
124. Teraoka Y, Zhang HM, Furukawa S, Yamazoe N (1985) Chem Lett 1743
125. Fukunaga H, Koyama M, Takahashi N, Wen C, Yamada K (2000) Solid State Ionics 132:279
126. Ishihara T, Honda M, Shibayama T, Minami H, Nishiguchi H, Takita Y (1998) J Electrochem Soc 145:3177
127. Shao ZP, Yang WS, Cong Y, Dong H, Tong JH, Xiong GX (2000) J Membr Sci 172:177
128. Shao ZP, Haile SM (2004) Nature 431:170
129. Pena-Martinez J, Marrero-Lopez D, Perez-Coll D, Ruiz-Morales JC, Nunez P (2007) Electrochim Acta 52:2950
130. Wei B, Lu Z, Huang X et al (2006) J Eur Ceram Soc 26:2827
131. Svarcova S, Wiik K, Tolchard J, Bouwmeester HJM, Grande T (2008) Solid State Ionics 178:1787
132. Arnold M, Gesing TM, Martynczuk J, Feldhoff A (2008) Chem Mater 20:5851
133. Yang Z, Martynczuk J, Efimov K et al (2011) Chem Mater 23:3169
134. Yan A, Cheng M, Dong YL et al (2006) Appl Catal B 66:64
135. Mizusaki J, Sasamoto T, Cannon WR, Bowen HK (1982) J Am Ceram Soc 65:363
136. Mizusaki J, Sasamoto T, Cannon WR, Bowen HK (1983) J Am Ceram Soc 66:247
137. Ralph JM, Rossignol C, Kumar R (2003) J Electrochem Soc 150:A1518
138. Kharton VV, Kovalevsk AV, Patrakeev MV et al (2008) Chem Mater 20:6457
139. Vidal K, Rodriguez-Martinez LM, Ortega-San-Martin L et al (2009) J Power Sources 192:175
140. Kuscer D, Hanzel D, Holc J, Hrovat M, Kolar D (2001) J Am Ceram Soc 84:1148
141. Kharton VV, Yaremchenko AA, Patrakeev MV, Naumovich EN, Marques FMB (2003) J Eur Ceram Soc 23:1417
142. Juste E, Julian A, Etchegoyen G et al (2008) J Membr Sci 319:185
143. Chiba R, Yoshimura F, Sakurai Y (1999) Solid State Ionics 124:281
144. Kharton VV, Viskup AP, Naumovich EN, Tikhonovich VN (1999) Mater Res Bull 34:1311
145. Kammer K, Mikkelsen L, Bilde-Sorensen JB (2006) J Solid State Electrochem 10:934
146. Tsipis EV, Kiselev EA, Kolotygin VA, Waerenborgh JC, Cherepanov VA, Kharton VV (2008) Solid State Ionics 179:2170
147. Takahashi S, Nishimoto S, Matsuda M, Miyake M (2010) J Am Ceram Soc 93:2329
148. Amow G, Skinner SJ (2006) J Solid State Electrochem 10:538
149. Amow G, Davidson IJ, Skinner SJ (2006) Solid State Ionics 177:1205
150. Greenblatt M, Zhang Z, Whangbo MH (1997) Synthetic Met 85:1451
151. Greenblatt M (1997) Solid State Mater Sci 174
152. Kobayashi Y, Taniguchi S, Kasai M, Sato M, Nishioka T, Kontani M (1996) J Phys Soc Jpn 65:3978
153. Zhang Z, Greenblatt M (1995) J Solid State Chem 117:236
154. Zhang Z, Greenblatt M, Goodenough JB (1994) J Solid State Chem 108:402
155. Greenblatt M, Zhang Z (1994) Abstr Pap Am Chem S 208:585
156. Perez-Coll D, Aguadero A, Escudero MJ, Daza L (2009) J Power Sources 192:2
157. Nedilko SA, Kulichenko VA, Dziazko AG, Zenkovich EG (2004) J Alloy Compd 367:251
158. Carvalho MD, Wattiaux A, Bassat JM et al (2003) J Solid State Electrochem 7:700
159. Carvalho MD, Cruz MM, Wattiaux A, Bassat JM, Costa FMA, Godinho M (2000) J Appl Phys 88:544
160. Bassat JM, Odier P, Villesuzanne A, Marin C, Pouchard M (2004) Solid State Ionics 167:341
161. Jorgensen JD, Dabrowski B, Pei S, Richards DR, Hinks DG (1989) Phys Rev B 40:2187
162. Bassat JM, Gervais F, Odier P, Loup JP (1989) Mater Sci Eng B 3:507
163. Sayagués MJ, Vallet-Regí M, Hutchison JL, González-Calbet JM (1996) J Solid State Chem 125:133
164. Boehm E, Bassat JM, Dordor P, Mauvy F, Grenier JC, Stevens P (2005) Solid State Ionics 176:2717
165. Munnings CN, Skinner SJ, Amow G, Whitfield PS, Davidson IJ (2005) Solid State Ionics 176:1895
166. Opila EJ, Tuller HL, Wuensch BJ, Maier J (1993) J Am Ceram Soc 76:2363
167. Burriel M, Garcia G, Santiso J, Kilner JA, Chater RJ, Skinner SJ (2008) J Mater Chem 18:416

168. Minervini L, Grimes RW, Kilner JA, Sickafus KE (2000) J Mater Chem 10:2349
169. Frayret C, Villesuzanne A, Pouchard M (2005) Chem Mater 17:6538
170. Chroneos A, Parfitt D, Kilner JA, Grimes RW (2010) J Mater Chem 20:266
171. Tsipis EV, Kharton VV (2007) J Solid State Electrochem 12:1039
172. Sun C, Hui R, Roller J (2010) J Solid State Electrochem 14:1125
173. Skinner S, Munnings CN, Amow G, Whitfield P, Davison I (2003) In: Singhal SC, Dokiya M (eds) SOFC VIII. Electrochemical Socciety Series, Pennington, NJ, USA, pp 552
174. Kharton VV, Yaremchenko AA, Tsipis EV, Frade JR (2003) In: Singhal SC, Dokiya M (eds) SOFC VIII. Electrochemical Society Series, Pennington, NJ, USA, pp 561
175. Sayers R, Liu J, Rustumji B, Skinner SJ (2008) Fuel Cells 8:338
176. Bae JM, Steele BCH (1999) J Electroceram 3:37
177. Jaiswal A, Wachsman ED (2005) J Electrochem Soc 152:A787
178. Zhong Z (2006) Electrochem Solid-State Lett 9:A215
179. Takeda T, Kanno R, Kawamoto Y, Takeda Y, Yamamoto O (2000) J Electrochem Soc 147:1730
180. Doshi R, Richards VL, Carter JD, Wang X, Krumpelt M (1999) J Electrochem Soc 146:1273
181. Díaz-Guillén JA, Díaz-Guillén MR, Padmasree KP, Fuentes AF, Santamaría J, León C (2008) Solid State Ionics 179:2160
182. Martínez-Coronado R, Aguadero A, de la Calle C, Fernández MT, Alonso JA (2011) J Power Sources 196:4181
183. Señarís-Rodríguez MA, Goodenough JB (1995) J Solid State Chem 118:323
184. Kim JH, Manthiram A (2010) Chem Mater 22:822
185. Kim JH, Kim YN, Cho SM, Wang H, Manthiram A (2010) Electrochim Acta 55:5312
186. Kim J-H, Kim YN, Bi Z, Manthiram A, Paranthaman MP, Huq A (2011) Electrochim Acta 56:5740
187. Kim YN, Kim J-H, Manthiram A (2011) Int J Hydrogen Energ
188. Vert VB, Serra JM, Jordá JL (2010) Electrochem Commun 12:278
189. Vannier RN, Skinner SJ, Chater RJ, Kilner JA, Mairesse G (2003) Solid State Ionics 160:85
190. Xia C, Liu M (2002) Adv Mater 14:521
191. Yang T, Li F, Xia D (2010) J Power Sources 195:2514
192. Xia C (2003) Appl Phys Lett 82:901
193. Camaratta M, Wachsman E (2007) Solid State Ionics 178:1242
194. Camaratta M, Wachsman E (2007) Solid State Ionics 178:1411
195. Li J, Wang S, Liu R, Wang Z, Qian JQ (2008) Solid State Ionics 179:1597
196. Ehora G, Daviero-Minaud S, Colmont M, Andre G, Mentre O (2007) Chem Mater 19:2180
197. Rolle A, Preux N, Ehora G, Mentré O, Daviero-Minaud S (2011) Solid State Ionics 184:31
198. Wang WG, Mogensen M (2005) Solid State Ionics 176:457
199. Liu B, Gu Y, Kong L, Zhang Y (2008) J Power Sources 185:946
200. Liu H, Zhu X, Cheng M, Cong Y, Yang W (2011) Chem Commun 47:2378
201. Lessing PA (2007) J Mater Sci 42:3465. doi:10.1007/s10853-006-0409-9
202. Ni M, Leung MKH, Leung DYC (2008) Int J Hydrogen Energ 33:2337
203. Herring JS, O'Brien JE, Stoots CM, Hawkes GL, Hartvigsen JJ, Shahnam M (2007) Int J Hydrogen Energ 32:440
204. Yang X, Irvine JTS (2008) J Mater Chem 18:2349
205. Eguchi K, Hatagishi T, Arai H (1996) Solid State Ionics 86–8:1245
206. Marina OA, Pederson LR, Williams MC et al (2007) J Electrochem Soci 154:B452
207. Osada N, Uchida H, Watanabe M (2006) J Electrochem Soc 153:A816
208. Brisse A, Schefold J, Zahid M (2008) Int J Hydrogen Energ 33:5375
209. Laguna-Bercero MA, Skinner SJ, Kilner JA (2009) J Power Sources 192:126
210. Jacobson AJ (2010) Chem Mater 22:660
211. Kuharuangrong S (2004) Ceram Intern 30:273
212. Boehm E, Bassat JM, Steil MC, Dordor P, Mauvy F, Grenier JC (2003) Solid State Sciences 5:973
213. Sayers R (2010) PhD Thesis, Imperial College London, London
214. Wang WS, Huang YY, Jung SW, Vohs JM, Gorte RJ (2006) J Electrochem Soc 153:A2066
215. Tsoga A, Gupta A, Naoumidis A, Nikolopoulos P (2000) Acta Mater 48:4709
216. Laguna-Bercero MA, Kilner JA, Skinner SJ (2010) Chem Mater 22:1134
217. Yu B, Zhang W, Xu J, Chen J (2010) Int J Hydrogen Energ 35:2829
218. Munnings CN, Skinner SJ, Amow G, Whitfield PS, Davidson IJ (2005) Solid State Ionics 176:1895
219. Aguadero A, Alonso JA, Fernandez-Diaz MT, Escudero MJ, Daza L (2007) J Power Sources 169:17
220. Kao CF, Jeng CL (2000) Ceram Intern 26:237
221. Rieu M, Sayers R, Laguna-Bercero MA, Skinner SJ, Lenormand P, Ansart F (2010) J Electrochem Soc 157:B477
222. Sayers R, Rieu M, Lenormand F, Kilner J, Skinner S (2011) Solid State Ionics 192:531
223. Perez-Coll D, Aguadero A, Escudero MJ, Daza L (2009) J Power Sources 192:2
224. Aguadero A, Escudero MJ, Perez M, Alonso JA, Daza L (2007) J.Fuel Cell Sci Techn 4:294
225. Aguadero A, Perez M, Alonso JA, Daza L (2005) J Power Sources 151:52
226. Adler SB (2004) Chem Rev 104:4791
227. Litzelman SJ, Hertz JL, Jung W, Tuller HL (2008) Fuel Cells 8:294
228. Pederson LR, Singh P, Zhou XD (2006) Vacuum 80:1066
229. Santiso J, Burriel M (2010) J Solid State Electrochem 15:985
230. Baumann FS, Fleig J, Cristiani G, Stuhlhofer B, Habermeier HU, Maier J (2007) J Electrochem Soc 154:B931
231. Kim G, Wang S, Jacobson AJ, Chen CL (2006) Solid State Ionics 177:1461
232. Kim GT, Wang SY, Jacobson AJ, Yuan Z, Chen CL (2007) J Mater Chem 17:1316
233. Garcia G, Burriel M, Bonanos N, Santiso J (2008) J Electrochem Soc 155:P28
234. Boehm E, Bassat JM, Steil MC, Dordor P, Mauvy F, Grenier JC (2003) Solid State Sci 5:973
235. Dembinski K, Bassat JM, Coutures JP, Odier P (1987) J Mater Sci Lett 6:1365
236. Burriel M, Santiso J, Rossell MD, Van Tendeloo G, Figueras A, Garcia G (2008) J Phys Chem C 112:10982
237. Raju AR, Aiyer HN, Rao CNR (1995) Chem Mater 7:225
238. Burriel M, Garcia G, Rossell MD, Figueras A, Van Tendeloo G, Santiso J (2007) Chem Mater 19:4056
239. Sase M, Hermes F, Yashiro K et al (2008) J Electrochem Soc 155:B793
240. Crumlin EJ, Mutoro E, Ahn S-J, et al (2010) J Phys Chem Lett 3149
241. Yamada A, Suzuki Y, Saka K et al (2008) Adv Mater 20:4124
242. Dragan MA (2006) PhD Thesis, RWTH Aachen